# Investigations on the dynamic behaviour of an on-board rotor-AMB system with touchdown bearing contacts: modelling and experimentation

Clément Jarroux, Jarir Mahfoud, Régis Dufour, Franck Legrand, Benjamin Defoy, Thomas Alban

# Investigations on the dynamic behaviour of an on-board rotor-AMB system with touchdown bearing contacts: modelling and experimentation

Clément Jarroux[a,*], Jarir Mahfoud[a], Régis Dufour[a], Franck Legrand[a], Benjamin Defoy[b], Thomas Alban[b]

[a] *University of Lyon, INSA Lyon, CNRS UMR5259, LaMCoS, Villeurbanne F-69621, France*
[b] *Baker Hughes, a GE company BHGE, 480 Avenue Gustave Eiffel, Le Creusot 71200, France*

**Abstract**

Active magnetic bearing (AMB) technology provides to rotating machinery, high operating speeds, direct couplings, almost frictionless support and a reduced footprint. In case of strong base excitations, the rotor may contact its touchdown bearings (TDBs), which are used as landing and safety bearings, while AMBs still operate. The paper presents, experimentally and numerically, this particular operating conditions where sliding friction-induced vibrations or AMB instabilities might be triggered. For this purpose, the developed finite-element model of the rotor-AMB-TDB system is experimentally validated using a lab-scale rotor test rig mounted on shaker. The validation is first conducted with no base excitation by analysing the mass unbalance responses and drop onto TDBs. In the presence of harmonic then impulse base excitations, the mass unbalance response are analysed in time and frequency domains. Considering harmonic tests, particular combinations of base motions and rotordynamics are observed depending on the frequency ratio between the base motion and the speed of rotation. TDB interactions produce rotor orbits flattening. The impulse tests highlight the friction effects and short periods of backward whirl are observed just after the contact. Despite some transient instabilities, the controller was always able to maintain the system stable by bringing damping. At each of these steps, the model reliability is assessed and predictions are close to the measured phenomena.

*Keywords:* Rotordynamics, Active magnetic bearing, On-board rotor, Touchdown bearing, Rotor-stator interaction

## 1. Introduction

Global energy consumption constantly grows and turbomachinery have a crucial role in energy conversion. Depending on the desired applications, the external environment, such as swell, cobblestone road, or earthquake may be critical to their dynamic behaviour, affecting their operability and maintainability. In order to guaranty such performances, the research investigations of the base motion effects on rotordynamics have begun since mid 1980s.

Earthquake may be approximated by non-stationary random process such as the Monte Carlo method and the effect of this kind of excitations on rotordynamics was studied in references [1–4]. Even if the shaft-bearing system natural frequencies are generally higher than the representative frequency of earthquake, the rotordynamics may become unstable when supported by oil-film bearings. Lee *et al.* [5] studied, numerically and experimentally, the effects of vertical shock on a rotor-bearing system and showed that amplifications of the rotor response are to be expected when the shock impulse is close to a system natural frequency.

Support rotations yielding parametric excitations may generate complex rotordynamics. At some specific support angular frequency, combined with the rotor-bearing system natural frequencies, instability zones are

*Corresponding author
*Email address:* clement.jarroux@gmail.com (Clément Jarroux)

exhibited and their surfaces depend on the angle amplitude, as shown in [6–10]. The use of magnetic forces, through actuators, may overcome these instabilities by making the system stiffer using a PD feedforward loop, as demonstrated by Das *et al.* [11], or using various control strategies as shown by Soni *et al.* [12].

The combined effects of support and shaft rotations were analysed previously by [6, 10, 13–15]. The rotor orbits may be fixed and perfectly periodic or quasi-periodic with more complex shapes depending on the ratio of the support angular frequency over the shaft speed of rotation. In case of high loads, the analysis of base motions combined with nonlinear bearing restoring forces exhibits the specific features of nonlinear dynamics, such as periodic, quasi-periodic or even chaotic regimes.

On the other hand, the use of active magnetic bearings (AMBs) is rising in industrial applications due to reduced costs but also to the improvement of electronic hardware performance and reliability. In addition to being an almost frictionless solution without lubrication device, it is convenient for high rotor speeds and a reduced system installation footprint. Being inherently unstable, the main difficulty is to develop the proper controller managing AMBs, see [16]. A wide variety of control strategies exist and most often, the conventional proportional-integral-derivative (PID) controller is employed in industrial applications. The use of touchdown bearings (TDBs) is systematic in rotor-AMB systems. These components are crucial to ensure safety in non-nominal operating conditions. They provide a support during transportation and a mechanical protection for AMBs against too large rotor deflection amplitudes due to aerodynamic overload or base motions. In case of magnetic levitation loss, the rotor is forced by gravity to drop onto its touchdown bearings, ensuring a back-up support. This transient phenomenon has been intensively analysed in the literature, see references [17–26] for more details. TDBs are generally composed of cageless ball bearings, comprising one or two rows, limiting the emergence of dangerous rotor behaviours induced by sliding friction. In most industrial designs, TDBs are fitted into the stator through compliant mountings. Ribbon damper technology has been widely adopted in modern designs. It is made of a corrugated steel foil and permits limiting the transmitted loads and brings stability, with a properly designed stiffness and damping respectively, when interactions with the rotor occur.

The effects of base motion on rotor-AMB systems are studied since the end of 90s when Murai *et al.* [27] analysed the response to earthquake excitation. Since then, some works were dedicated to the implementation of control strategies to overcome these base motions and avoid TDBs interactions.

An effective solution is to implement a feedforward compensator added to a conventional feedback loop, as shown by Matsushita *et al.* [28] where the vibration amplitudes of a rotor-AMB system subjected to Kobe earthquake were reduced by 60 %. Using less control current, Suzuki [29] implemented the infinite impulse response filter as feedforward control loop and showed that the rotor response could be reduced about the half of the response only using PID. Nonlinear dynamic systems generate sub and super harmonic responses when subjected to harmonic forcing. Based on this observation, Marx and Nataraj [30] developed a feedforward loop, where the correction current was set to be a sum of multiples and fractions of the base motion frequency. The acceleration feedforward compensation appears to be also effective in Kang and Yoon [31] to limit harmonic base motions for applications such as electro-optical sight mounted on a moving vehicle. The compensator was designed experimentally thanks to the filtered-x least mean square algorithm, which was also used by Kim *et al.* [32].

Other works emphasized mostly on the AMB feedback control loop adapted to limit base motions. Kang *et al.* [33] used the sliding mode control, which was able to achieve high performance robust control against parameter uncertainties and external disturbances. The effect of an horizontal impact was analysed by Cole *et al.* [34]. Three control strategies were developed to reduce the direct forcing as well as the motions of the support. If the controller was not suitable, the base motion generated rotor-TDB contacts. Some control strategies, however, can limit or even prevent the rotor-stator interaction such as the $H_\infty$ controller according to Keogh *et al.* [35]. The combined $wavelet - H_\infty$ controller gives the best performance in terms of transmitted forces and vibration limitations. The case of base rotations control was investigated by Maruyama *et al.* [36] where the stator motions, integrated as rotation disturbances, acted on the rotor-stator relatives angles. The dynamic behaviour of on-board rotor-AMB system was numerically investigated by Jarroux *et al.* [37], considering rotation and translation motions of the base. The model was validated using previous experimental results where angular shocks were applied to a flexible rotor with high gyroscopic effects supported by conventional ball bearings.

Most of AMB controllers employed in industrial applications are of PID type, without any base disturbance consideration. Therefore, some works analysed the effects of base disturbances when the control strategy was not specifically tuned for that purpose. Hawkins *et al.* [38] tested a vertical flywheel-AMB system subjected to translational shocks for transit bus applications. Even if the controller was not specifically tuned for base disturbance rejections, it was able to maintain the rotor and no TDB contact occurred. The use of a shock isolator permitted reducing the transmitted axial shock by 65 %, corresponding with the work of Leilei *et al.* [39]: using flexible supporting conditions, base disturbance rejection of rotor-AMB system can be improved. Hawkins *et al.* [40] presented an experimental and numerical comparison of a magnetic bearing supported shipboard compressor subjected to sinusoidal translation up to 1.5 G. The vibration requirements were in accordance with MIL-STD-167 standards. AMBs remained in their linear range during these tests. This was not the case in the work of Kasarda *et al.* [41] where a non-rotating mass mounted on magnetic bearings controlled by PID feedback and subjected to a sinusoidal base motion was analysed numerically and experimentally. In case of extremely low damping, nonlinear dynamics responses were observed.

In most of these previous studies, the rotor responses due to base motions remained limited and were not sufficient to generate contact with the TDBs, either because a specific control strategy was applied to reject external disturbances or because the acceleration levels tested remained quite small. However, in case of large foundation displacements, rotor-TDBs contacts could occur while AMBs still operate. Indeed, even if the conventional procedure is to stop the machine in few seconds when the rotor displacements exceed a designed threshold, the dynamic behaviour of the shaft during this phase remains quite unknown and potential instabilities may be triggered. For example, the sliding friction forces produced at the rotor-TDB interface could lead to dangerous rotordynamics such as backward whirl followed by dry whip. More details about rotor-stator interactions and the wide variety of induced dynamic regimes, are provided in references [42–52]. On the other hand, AMBs could destabilise the rotor by producing negative damping forces due to the emergence of undamped frequencies.

The literature shows few studies regarding the combined effect of base motions, TDB contact nonlinearities and magnetic forces on rotordynamics. Hawkins [53] studied numerically the transient dynamic behaviour of a rotor supported by homopolar permanent magnet bias magnetic bearings subject to vertical shocks and TDB contact interactions. More recently, Hawkins *et al.* [54] analysed the effect of shock and TDB contacts on a magnetic bearing supported chiller compressor. After short period of rebounds, the rotor recovered its centered position and no particular damages were notified after the tests. Jarroux *et al.* [55] also investigated those aspects and it was shown that the dynamic behaviour of the system remains mostly stable after rotor-TDB interactions. Su *et al.* [56] numerically analysed the effects of TDB contact parameters onto the dynamic behaviour of a rigid rotor supported on AMBs subjected to strong base motion (up to 20 G). Periodic, nT-periodic, quasi-periodic responses as well as jump phenomena are revealed.

The presented work is a contribution to the understanding of complex phenomena associated with the dynamic behaviour of turbomachinery supported by AMBs facing critical external events. In particular, it investigates the flexible rotordynamics exhibited when the effects of mass unbalance forces, rigid base motions and TDBs contact are combined while AMBs still operate. The numerical and experimental analyses are conducted both with harmonic and impulse foundation motions in vertical translation.

First is developed the modelling approach, using the finite-element method, required to perform the transient and nonlinear simulations. Then, the experimental set-up, comprising the lab-scale rotor-AMB system test rig mounted on a 6-DOF shaker, is described. Before carrying on base motion tests, two steps of validation are performed. At each step, the observed phenomena are explained, the numerical model is assessed and the prediction-measurement correlation is discussed.

## 2. On-board rotor-AMB system modelling

The different parts of the numerical model required to perform nonlinear and transient simulations are presented in the following subsections. The on-board flexible rotor, the AMB and the TDB models are described separately. A typical rotor-AMB system is sketched in Fig. 1.

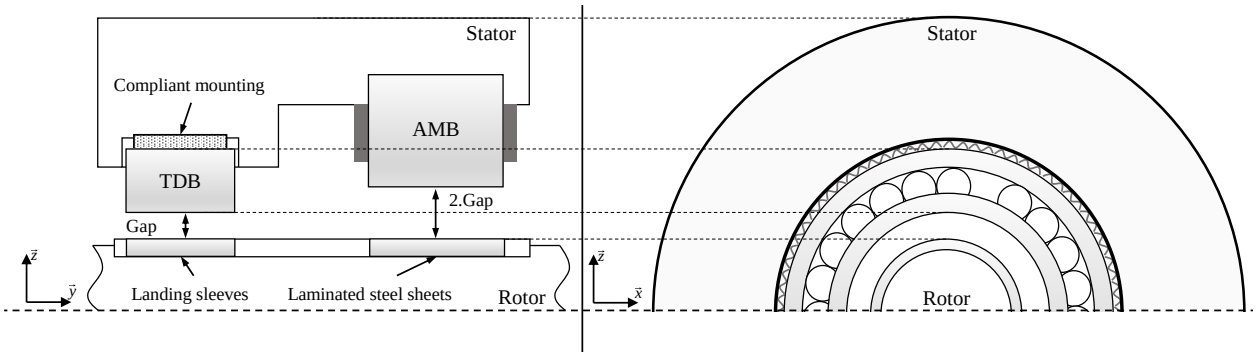


Figure 1: AMB and TDB assembly

### *2.1. On-board flexible rotor model*

The effects of flexible support on rotordynamics was analysed by Cavalca *et al.* [57]. However generally speaking, the stator of industrial turbomachinery support is very stiff in comparison with the rotor. In this investigation, the support is assumed to be rigid but movable.

Considering the six motions of the rigid support, see Fig. 2, implies deep changes into the energy formulations of rotor components, such as disc, shaft, mass unbalance distribution and finally, into the equations of motion. In what follows, only the main guidelines are given on the derivation of the rotordynamics equations of motion in bending taking into account the FE method and the effect of the base motion. For more details about the mechanical modelling, the matrices and vectors formulations, readers shall refer to the references [6–8].

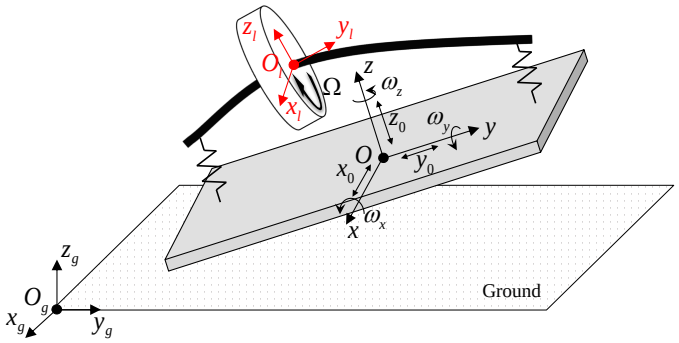


Figure 2: On-board rotor - set-up of the different frames of references

The proposed model requires the use of three distinct frames of reference to set-up correctly the equations of motion. The rotor neutral line deflections, represented by the non-inertial local frame $R_l\,(x_l, y_l, z_l)$, are described with respect to the rigid support, referred to as the non-inertial frame $R\,(x, y, z)$, as for conventional rotordynamics. The motions of this rigid support are described with respect to the ground, Galilean or inertial frame, called $R_g\,(x_g, y_g, z_g)$. The rotor deflections are therefore always described relatively to the support motions which makes it easy to integrate any type of bearings. Then, the method to derive the equations of motion is identical to the one proposed by Lalanne and Ferraris [58], for conventional rotordynamics. Once the frames of reference established, the formulation of vectors describing the relative motions between each others is determined: the instantaneous angular velocity vector $\overrightarrow{\omega}_R^{R_g}$ and the position vector

$\overrightarrow{O_gO}$ are needed. These vectors are expressed in Eq. (1), with respect to $R_g$ in $R$.

$$\overrightarrow{O_gO} = \begin{Bmatrix} x_0 \\ y_0 \\ z_0 \end{Bmatrix}_R ; \overrightarrow{\omega}_R^{R_g} = \begin{Bmatrix} \omega_x \\ \omega_y \\ \omega_z \end{Bmatrix}_R \tag{1}$$

where $x_0, y_0, z_0$ and $\omega_x, \omega_y, \omega_z$ are the positions and the instantaneous angular velocities of the base, described in Fig. 2. The energies or the virtual work of each component is then calculated: the flexible shaft modelled Timoshenko beam element, comprising 4-DOFs per node, contributes with its kinetic and strain energies, the one-node rigid disc element as well as the discrete mass unbalance with their kinetic energies, and the bearing with the virtual work of its restoring forces. The different contributions of the base are expressed in $R$ in motion with respect to $R_g$. The base motions modify only the kinetic energies.

Once the elementary energies are gathered, they are derived by using the Lagrange's equations:

$$\frac{d}{dt}\left(\frac{\partial T}{\partial \dot{\delta}_i}\right) - \frac{\partial T}{\partial \delta_i} + \frac{\partial U}{\partial \delta_i} = F_{\delta_i} \tag{2}$$

with $\delta_i$ a DOF of the system, $T$ and $U$, the kinetic and strain energies, respectively, and $F_{\delta_i}$ the external force applied to the DOF $\delta_i$. The equations of motion are obtained as follows:

$$\begin{aligned} M\ddot{\delta} + \left(\Omega C_G + \omega_y C_{\omega_y}^{bm}\right)\dot{\delta} + (K + \dot{\Omega} K_G + \dot{\omega}_y K_{\dot{\omega}_y}^{bm} + \Omega\, \omega_y K_{\Omega\omega_y}^{bm} + \omega_{x^2} K_{\omega_{x^2}}^{bm} + \\ \omega_{y^2} K_{\omega_{y^2}}^{bm} + \omega_{z^2} K_{\omega_{z^2}}^{bm} + \omega_x \omega_z K_{\omega_x\omega_z}^{bm})\,\delta = F_{mu} + F_{bm} + F_g + F_{amb} + F_c \end{aligned} \tag{3}$$

where $M$, $K$ and $C_G$ are respectively the mass, the structural stiffness and the gyroscopic matrices. The effects of the variable speed of rotation $\Omega$ are considered in the stiffness matrix $K_G$, see Bouziani and Ouelaa [13]. The vector $\delta$ gathers all the DOFs of the mesh. The superscript $bm$ stands for the base motion effects. The support rotations bring $C_\omega^{bm}, K_\omega^{bm}$, the additional gyroscopic and stiffness matrices which are responsible for parametric excitations, leading to potential lateral instabilities. The external force vector $F_{bm}$ includes the support translation effects combined with rotations, $F_{mu}$ is the mass unbalance force vector taking into account the normal centrifugal forces and the tangential effects associated with a variable speed of rotation. The effect of gravity is considered in $F_g$. The external force vectors $F_{amb}$ and $F_c$ represent the AMBs and the TDBs contact forces respectively. They are developed in the next section.

The modal superposition method is employed to perform low computational time simulations with a reduced system of equations while maintaining high reliability. A modal truncation is realised and the first ten mode shapes are chosen in order to reduced the modal equations to be solved. The damping is introduced through the modal damping ratio $\alpha_\psi$ evaluated from experimental modal analysis and the modal damping matrix $C_\psi$ is written as:

$$C_\psi = 2\alpha_\psi \sqrt{K_\psi M_\psi} \tag{4}$$

To perform transient simulations using RK5 scheme, the Eq. (3), projected into the modal basis, is rewritten in its state space form Eq. (5). The subscript $\psi$ stands for matrices and vectors established in the modal base. For practical reasons, the time dependent and parametric matrices are considered as external forces and placed in the second member.

$$\begin{cases} \dot{X} = AX + BU \\ Y = CX + DU \end{cases} \tag{5}$$

where $X$ is the state vector, $q$ is the modal variable vector and $A$ the matrix of the system dynamics, such as:

$$X = \begin{Bmatrix} q \\ \dot{q} \end{Bmatrix} \tag{6}$$

$$A = \begin{bmatrix} 0 & I \\ -M_{\psi}^{-1} K_{\psi} & -M_{\psi}^{-1} C_{\psi} \end{bmatrix} \tag{7}$$

$B$ is the input matrix and $U$ is the input vector comprising the forces applied to the system, such as:

$$B = \begin{bmatrix} 0 \\ M_{\psi}^{-1} \end{bmatrix} \tag{8}$$

$$\begin{gathered} U = -\left(\Omega C_{G,\psi} + \omega_y C^{bm}_{\omega_y,\psi}\right) \dot{q} - \left( \dot{\Omega} K_{G,\psi} + \dot{\omega}_y K^{bm}_{\dot{\omega}_y,\psi} + \right. \\ \left. \Omega\ \omega_y K^{bm}_{\Omega\omega_y,\psi} + \omega_{x^2} K^{bm}_{\omega_{x^2},\psi} + \omega_{y^2} K^{bm}_{\omega_{y^2},\psi} + \omega_{z^2} K^{bm}_{\omega_{z^2},\psi} + \omega_x \omega_z K^{bm}_{\omega_x\omega_z,\psi} \right) q \\ + \psi^t \left(F_{mu} + F_{bm} + F_g + F_{amb} + F_c\right) \end{gathered} \tag{9}$$

Finally, $C$ is the output matrix and $Y$ is the output vector comprising the DOFs of interest. The matrix $D$ is the feedforward matrix and is zero in this study.

### *2.2. Active magnetic bearings model*

AMBs are used to levitate the rotor and the Fig. 3 recalls all the required electromechanical components, from the controller to the electromagnet, to generate the attractive magnetic force $f_{amb}$ along the action line. The control current $i_c$ is provided by the controller according to the measured rotor relative displacement

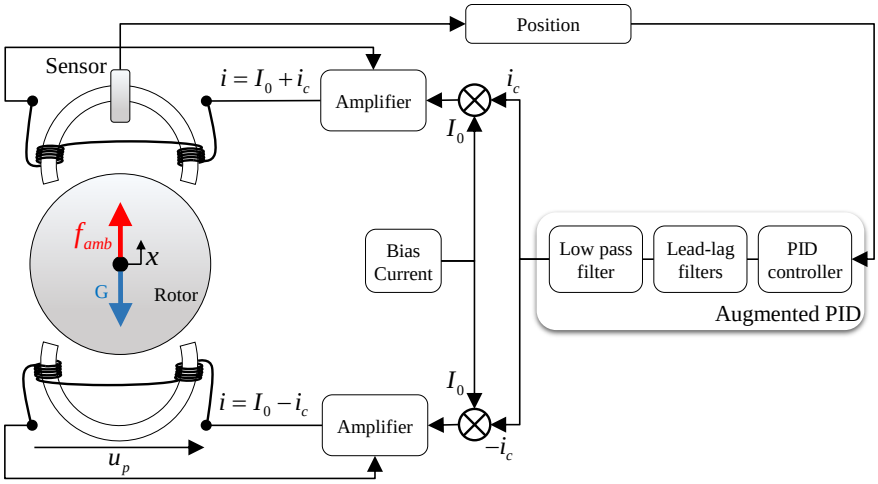


Figure 3: Sketch of AMB supporting the rotor

with respect to the centre of AMBs, $I_0$ and $u_p$ being respectively, the bias current and the coil voltage. The augmented PID is used for conventional rotordynamics since it remains the most employed in industrial application, due to its simplicity and robustness. The complete controller transfer function $G_{co}$ is provided in Eq. (10), in the Laplace domain.

$$G_{co} = G_{ampl} \times G_{so} \times G_{fo} \times G_{pid} \tag{10}$$

where $G_{ampl}$, $G_{so}$, $G_{fo}$ and $G_{pid}$ are respectively the amplifier, the second order lead-lag filter, the first order lead-lag filter and the PID transfer functions. The simplest way to formulate the PID transfer function is:

$$G_{pid}(s) = K_p + K_d s + \frac{K_i}{s} \tag{11}$$

The gain $K_p$ is equivalent to the controller stiffness and is chosen to counteract the inherent negative stiffness of AMBs. $K_i$ is the integral gain, it permits centering the rotor in the bearing. Finally, $K_d$ is the derivative gain, providing damping and stability into the system on the operating speed range. The first order lag filter is used to limit the increase of damping generated by the derivative gain. Indeed, a too large increase of phase on the operating speed range may imply a low stiffness and difficulty to limit the gain in higher frequency. Its transfer function $G_{fo}$ is given by:

$$G_{fo}(s) = \frac{s + 2\pi f_n}{s + 2\pi f_d} \tag{12}$$

where $f_n$ and $f_d$ are the numerator and denominator frequencies which characterized the filter.

The high frequency modes, outside the operating speed ranges but still comprised in the controller bandwidth are also damped to avoid spillover effect (high frequency instability). Second order lead-lag filters are used to this end, and the transfer function is given in Eq. (13). For robustness purpose, the gyroscopic effects on the different rotor modes are taken into account for the application of phase.

$$G_{so}(s) = \frac{s^2 + 2\xi_n (2\pi f_n)\, s + (2\pi f_n)^2}{s^2 + 2\xi_d (2\pi f_d)\, s + (2\pi f_d)^2} \tag{13}$$

with $f_n$, $f_d$ and $\xi_n$, $\xi_d$, the numerator, denominator filter frequencies and the damping ratios respectively.

The amplifier controls the electromagnet by applying the voltage $u_p$ on the coil, as shown in Fig. 3. Its transfer function $G_{ampl}$ is described with a first order low pass filter. Then, the electromagnet, used in differential driving mode for more stability, generates an attractive force, called $f_{amb}$, along the action line which adopts the following formula:

$$f_{amb} = 4\cos\alpha\mu_0 S N^2 \left[ \frac{(I_0 - i_c)^2}{\left(\frac{L}{\mu_r} + 2g_0 - 2x\cos\alpha\right)^2} - \frac{(I_0 + i_c)^2}{\left(\frac{L}{\mu_r} + 2g_0 + 2x\cos\alpha\right)^2} \right] \tag{14}$$

with $\mu_0$ and $\mu_r$ the vacuum and iron core magnetic permeabilities respectively, $S$ the pole area, $N$ the number of turns in one coil, $g_0$ the nominal air gap, $x$ the rotor position along the considered action line, $L$ the average length of the magnetic flux lines and $\alpha$ the angle between the action line and the line joining the pole and the rotor centres.

To compensate the base motions, the augmented PID controller may have to generate large control currents $i_c$ to counteract large rotor displacements $x$. For this reason, the AMB forces are not linearised as done usually and the amplifier saturation effects are taken into account.

### *2.3. Touchdown bearings model*

The modelling of TDBs have been extensively developed in the literature, especially in the context of magnetic levitation loss. As explained by Kärkkäinen *et al.* [22], the overall rotordynamics prediction of a turbomachinery using detailed models, where each rolling element has several DOF, is not necessary. The modelling approach is inspired by Schmied and Pradetto [18]. Though the ribbon damper has demonstrated dry friction damping under harmonic forcing, it was shown by Jarroux *et al.* [23] that a specific contact law using viscous damping could correctly describe the overall transient dynamics and transmitted loads of an industrial-scale rotor drop. The same modelling approach is employed in this work.

Rotor-TDB interactions generate a normal contact force $f_n$ and an induced friction force $\mu f_n$ in tangential direction, as shown in Fig. 4. The shaft first impacts the coupled ball bearing ribbon damper system in a series mode. Once the ribbon is completely crushed, it only has a static contribution and the rotor faces the ball bearing restoring force. The TDB model is characterized by softness, large damping and linear ball bearing when the ribbon is not crushed, then by high stiffness, low damping and nonlinear bearing when the ribbon is crushed. The rotor-TDB misalignments are considered since they can seriously affect the rotordynamics during contact, as shown by Halminen *et al.* [59] when analysing rotor drop response.

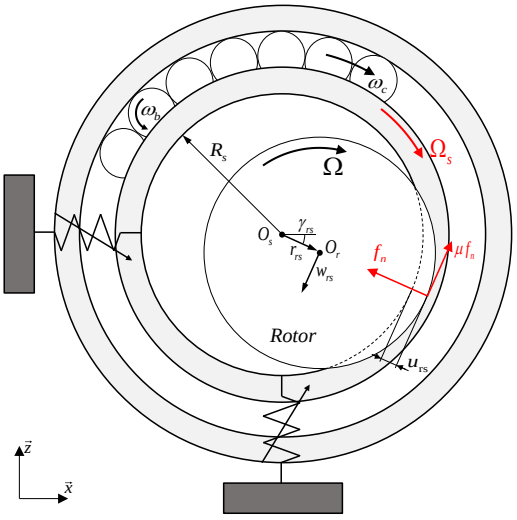


Figure 4: Sketch of the touchdown bearing model

The contact problem is solved using the penalty method and the related normal component $f_n$ is described in Eq. (15).

$$f_{\mathrm{n}}\left(u_{\mathrm{rs}}\right)=\begin{cases} f_{\mathrm{brg}}\left(u_{\mathrm{rs}}-u_{\mathrm{rd}}\right)+c_{\mathrm{brg}}\dot{u}_{\mathrm{rs}}+k_{\mathrm{eq}}u_{\mathrm{rd}} & ;u_{\mathrm{rs}}\geq u_{\mathrm{rd}} \\ k_{\mathrm{eq}}u_{\mathrm{rs}}+c_{\mathrm{eq}}\dot{u}_{\mathrm{rs}} & ;u_{\mathrm{rd}}>u_{\mathrm{rs}}\geq 0 \\ 0 & ;u_{\mathrm{rs}}<0 \end{cases} \tag{15}$$

with $u_{rs}, \dot{u}_{rs}$ the rotor-TDB normal relative clearance and its time derivative, in Eq. (16) and (17), where $x_r, z_r$, $x_s, z_s$ and $u_s$ are the rotor displacements, the TDB misalignments and the initial clearance respectively.

$$u_{rs}=r_{rs}-u_s=\sqrt{\left(x_r-x_s\right)^2+\left(z_r-z_s\right)^2}-u_s \tag{16}$$

$$\dot{u}_{rs}=\frac{du_{rs}}{dt}=\frac{\dot{x}_r\left(x_r-x_s\right)+\dot{z}_r\left(z_r-z_s\right)}{\sqrt{\left(x_r-x_s\right)^2+\left(z_r-z_s\right)^2}} \tag{17}$$

with $u_{rd}$ the ribbon crushing capacity, $k_{eq}$ and $c_{eq}$ the coupled ball bearing ribbon damper dynamic parameters considered in series mode and computed using the linearised ball bearing $k_{brg}$, $c_{brg}$. The ribbon damper has $k_{rd}$, $c_{rd}$ as dynamic parameters. The ball bearing restoring force $f_{brg}$ comes from the force-deflection relationship, obtained from analytical results based on [60, 61], as done in Jarroux *et al.* [23]. As it is difficult to predict the depth of penetration, these forces are conserved nonlinear.

The tangential component $f_t$, Eq. (18), applied on the rotor, considers the sliding friction force $\mu\left(v_s\right) f_n$ generated at the rotor-TDB interface due to different speeds of rotation, $v_s$ being the relative rotor-TDB sliding velocity. The tangential damping $c_t$ provided by the ribbon damper counteracting the relative rotor whirl velocity $w_{rs}$ is also taken into account.

$$f_{\mathrm{t}}\left(u_{\mathrm{rs}}\right)=\begin{cases} \mu\left(v_s\right) f_n & ;u_{\mathrm{rs}}\geq u_{\mathrm{rd}} \\ \mu\left(v_s\right) f_n-c_t w_{rs} & ;u_{\mathrm{rd}}>u_{\mathrm{rs}}\geq 0 \\ 0 & ;u_{\mathrm{rs}}<0 \end{cases} \tag{18}$$

where $w_{rs}$ is the relative whirl speed defined by Eq. (19) and where $\gamma_{rs}$ is the relative whirling angle given

by Eq. (20).

$$w_{rs} = r_{rs}\dot{\gamma}_{rs} = \frac{\dot{x}_r\left(z_r - z_s\right) - \dot{z}_r\left(x_r - x_s\right)}{\sqrt{\left(x_r - x_s\right)^2 + \left(z_r - z_s\right)^2}} \tag{19}$$

$$\gamma_{rs} = \arctan\left(\frac{z_r - z_s}{x_r - x_s}\right) \tag{20}$$

The sliding friction coefficient $\mu\left(v_s\right)$ is a polynomial formulation of the regularized Stribeck model, Eq. (21), used by Nguyen *et al.* [62].

$$\mu\left(v_s\right) = \frac{v_s}{2v_{ref}}\left(\frac{1 - \sqrt{1 - \frac{\mu_{dyn}}{\mu_{dry}}}}{1 + \frac{|v_s|}{2v_{ref}\mu_{dyn}}\left(1 - \sqrt{1 - \frac{\mu_{dyn}}{\mu_{dry}}}\right)} + \frac{1 + \sqrt{1 - \frac{\mu_{dyn}}{\mu_{dry}}}}{\left(1 + \frac{|v_s|}{2v_{ref}\mu_{dyn}}\left(1 - \sqrt{1 - \frac{\mu_{dyn}}{\mu_{dry}}}\right)\right)^2}\right) \tag{21}$$

where $\mu_{dry}$, $\mu_{dyn}$ being respectively the dry and the dynamic friction coefficient, depending on the value of the relative sliding velocity $v_s$. $v_{ref}$ is a numerical parameter that specifies the slope of the transition between two slip states in opposite direction.

In order to avoid discontinuities inherent to linear viscous damping in the contact force, arctangent laws are employed to regularize the normal $f_n$ and the tangential $f_n$ components when the relative clearance exceeds zero $u_{\mathrm{rd}} > u_{\mathrm{rs}} \geq 0$ and when it exceeds the ribbon crushing capacity $u_{\mathrm{rs}} \geq u_{\mathrm{rd}}$.

The TDBs are driven in rotation by the previously described sliding friction forces $\mu\left(v_s\right)$. The modelling approach assumes a perfect rolling-without-slipping kinematic condition. This assumption seems not too strong according to Helfert *et al.* [63]. They analysed with a rapid camera the rotation of the balls of a cageless TDB during a rotor drop and observed that the balls as well as the inner race reached the shaft speed almost at the same time: the sliding between the rolling elements has few influence on the time needed for the TDB to reach the rotor speed of rotation.

The rotational equation of motion is provided by:

$$J_{eq}\dot{\Omega}_s + \Phi\Omega_s = \mu\left(v_s\right) f_n R_s - M_f \tag{22}$$

with $\Omega_s$ the TDB speed of rotation, $M_f$ the resistive torque based on the Palmgren theory [64], $R_s$ the inner race radius and $\Phi$ the rotational damping used to break the bearing when no more external loads are present. Assuming a perfect rolling-without-slipping kinematic condition between balls and races, the equivalent rotational inertia $J_{eq}$, comprising balls and inner race, can be computed.

The complete numerical model is finally schemed in Fig. 5. Each modelling part developed in this section is represented by dedicated AMB, support motion and TDB blocks. All the contributions, not directly related to the rotor structure, are added as second members in the equations of motion. The approach is modular and each model can be employed or not in the simulations.

## 3. Test rig

The base motion experimentations are carried out using a lab-scale rotor-AMB system mounted on a 6-axis shaker.

### *3.1. Lab-scale rotor-AMB system*

The lab-scale rotor-AMB system, see Fig. 6, is composed of a standard steel rotor with an off centred disc and two identical radial AMBs called NDE (Non Driven End) and DE (Driven End) equipped with TDBs.

The 6.5 kg rotor is made of standard steel. It was designed to have its dynamic behaviour representative of a high-speed turbomachinery, without any bending modes in the operating speed range and low gyroscopic effects. The disc, 120 mm in diameter and 25 mm in thickness, is placed at two-third of the bearing span from the DE side. The rotor dimensions are provided in Fig. 6.

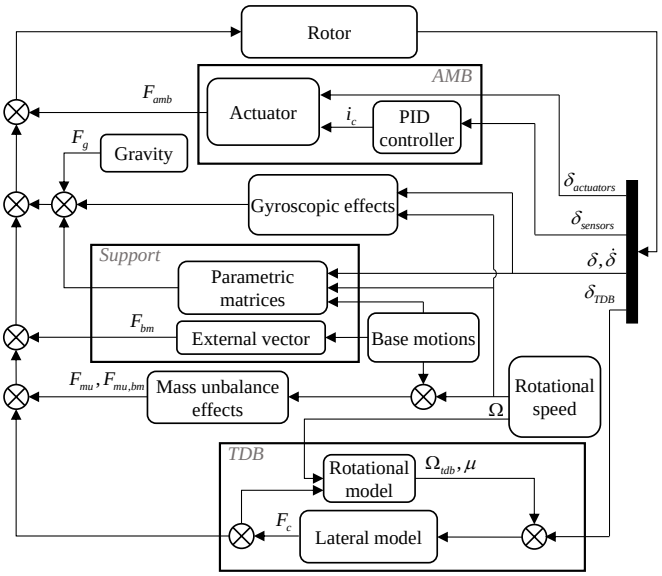


Figure 5: Diagram of the numerical model

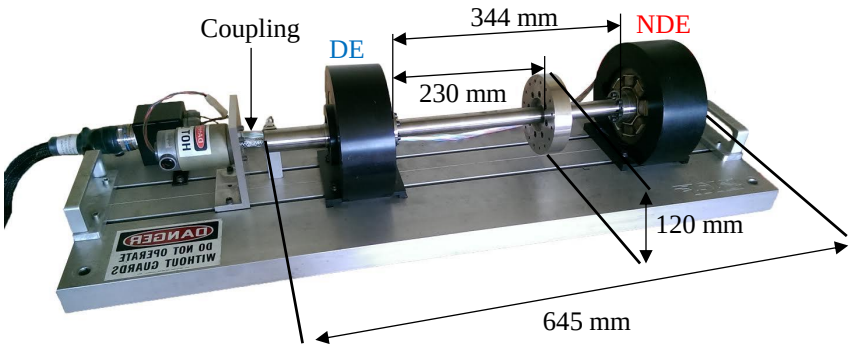


Figure 6: Lab-scale rotor test rig

The finite-element rotor model and its first three bending mode shapes at rest (fixed support, no speed of rotation) are sketched in Fig. 7. Table 1 gathers the evolution of the rotor natural frequencies with respect to the speed of rotation and shows the weak gyroscopic effects.

Table 1: Rotor natural frequencies in bending

| Modes | 0 rpm (Hz) | 15 000 rpm (Backward) (Hz) | 15 000 rpm (Forward) (Hz) |
|---|---|---|---|
| **Cylindrical** | 75 | 75 | 75 |
| **Conical** | 92 | 89 | 94 |
| **1** | 203 | 194 | 213 |
| **2** | 581 | 563 | 598 |
| **3** | 1 142 | 1 036 | 1 260 |

The rotor is driven by a 500 W electric motor through a flexible coupling, which also plays the role of axial thrust. The maximum operating speed was set to 9 500 rpm (160 Hz), which includes the first two

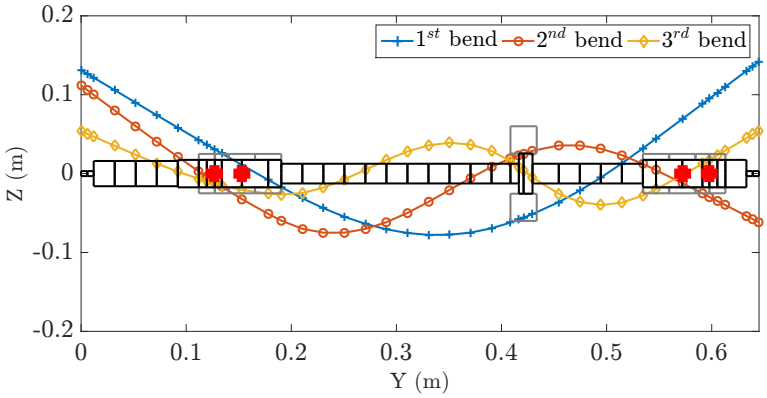


Figure 7: The finite-element rotor model and its first three bending mode shapes

suspension modes. The speed of rotation is measured by using a key phasor placed close to the motor.

The AMBs were manufactured by SKF® and designed in the configuration load between action line axes. Each of them has a maximum static capacity of 280 N with an air gaps of 0.432 mm. They are powered in differential driving mode with a bias current of 1 A. Pulse width modulator (PWM) amplifiers control the coil currents, provided in the range of [0-3] A. Two variable reluctance probes, integrated in the housing of each bearing, measure the rotor displacement. These sensors are non-colocalised with actuators which is considered in the augmented PID tuning. The AMB characteristics using the previously defined parameters are provided in Tab. 2.

Table 2: Active magnetic bearings properties

| **Parameter** | **Value** |
|---|---|
| Angle between the action line and the line joining the pole - $\alpha$ | $\frac{\pi}{8}$ |
| Pole area - $S$ | $233e^{-6}$ m$^2$ |
| Number of turns in one coil - $N$ | 138 |
| Magnetic air gap - $g_0$ | 0.432 mm |
| Average length of the magnetic flux lines - $L$ | 114 mm |

The AMBs are controlled with an augmented PID based on Eq. (10) and its complete transfer function is plotted in Fig. 8. Damping is brought over the operating speed range by applying a positive phase thanks to the derivative gain combined with a first order lag filter. Concerning high frequency range, the green rectangles indicate the bending mode positions and their thickness are related to the gyroscopic effects. To avoid spillover instabilities, positive phase is provided in these rectangles using second order lag filters. When a vibration node is placed between the sensor and the actuator, the phase is turned by 180 degrees, as for the third bending mode, at the NDE side, see Fig. 7.

The rotor-AMB system is equipped with two TDBs which are cageless single row deep groove ball bearings composed of nitrogen steel races and ceramics balls. They are fitted into the housing through a ribbon damper, characterized by its stiffness, damping and dynamic crushing capacity, see Tab. 3.

### *3.2. 6-DOF Shaker*

To perform base motion tests, the lab-scale rotor-AMB system is fixed on a 6-axis hydraulic shaker of 63 kN, as shown in Fig. 9. It is able to apply various combinations of solicitations along and around the 3 axes (translations and rotations) to a maximum payload of 450 kg in a range [0-250] Hz. A maximum acceleration of 10 G, $\pm$ 50 mm in translation and $\pm$ 4 degrees in rotation can be reached.

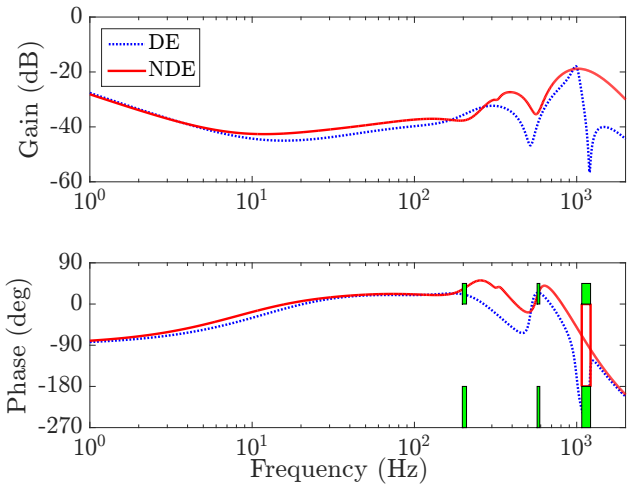


Figure 8: Controller transfer function - augmented PID

Table 3: Touchdown bearing properties

| **Parameter** | **Value** |
|---|---|
| NDE touchdown bearing measured clearance - $u_{snde}$ | 0.1 mm |
| DE touchdown bearing measured clearance - $u_{sde}$ | 0.11 mm |
| Pitch diameter - $d_m$ | 45.5 mm |
| Ball diameter - $D$ | 4.7 mm |
| Number of balls - $Z$ | 23 |
| Computed ball bearing static capacity - $C_S$ | 8200 N |
| Computed ball bearing equivalent inertia - $J_{eq}$ | $1.4e^{-5}$ kg.m$^2$ |
| Computed ball bearing stiffness - $k_{brg}$ | $1.5e^8$ N.m$^{-1}$ |
| Estimated ball bearing normal damping - $c_{brg}$ | $4e^2$ Ns.m$^{-1}$ |
| Computed ribbon stiffness - $k_{rd}$ | $3e^6$ N.m$^{-1}$ |
| Estimated ribbon normal damping - $c_{rd}$ | $1e^3$ Ns.m$^{-1}$ |
| Estimated ribbon tangential damping - $c_t$ | $5e^2$ Ns.m$^{-1}$ |
| Estimated ribbon crushing capacity - $u_{rd}$ | 0.02 mm |

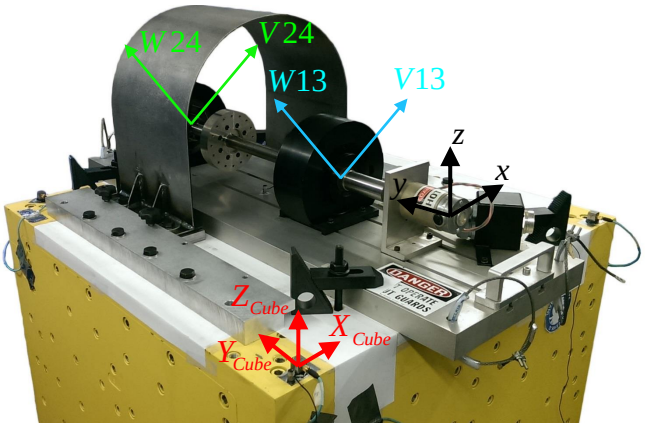


Figure 9: Rotor rig - Cube$^{TM}$ assembly - measuring sensors

Base motion tests were carried out considering harmonic and impulse test in vertical translation. The shaker stop was also recorded to analyse the capacity of the AMBs to control the rotor after contact situations. Base accelerations were recorded in the three directions (Xcube, Ycube, Zcube) using four tri-axial accelerometers fixed on the shaker. The displacement and current sensors for each action line (V13, W13, V24, W24), see 9, and the speed of rotation were also recorded. The sampling frequency was set to 24 756 Hz.

## 4. System identification

The base excitations is nil. Mass unbalance responses were first realised to identify the rotor-AMB system dynamics and assess the reliability of the numerical model predictions for simple linear test cases. Rotor drop response at rest were also performed since it is an efficient method to validate the TDB contact model.

### *4.1. Mass unbalance response*

The speed of rotation was slowly increased up to 9 500 rpm with a rate of 50 rpm per seconds. AMBs are considered linear for these simulations since rotor deflections are expected to be small. The numerical and experimental rotor synchronous responses, considering a 17 g.mm mass unbalance located at 0° of the key phasor top dead centre, are depicted in Fig. 10. Due to the symmetry of the rotor-AMB system the numerical are identical along V and W axes. Trends are identical in terms of vibration amplitudes and frequency position of the suspension modes. The deviations revealed at low speed, particularly visible at

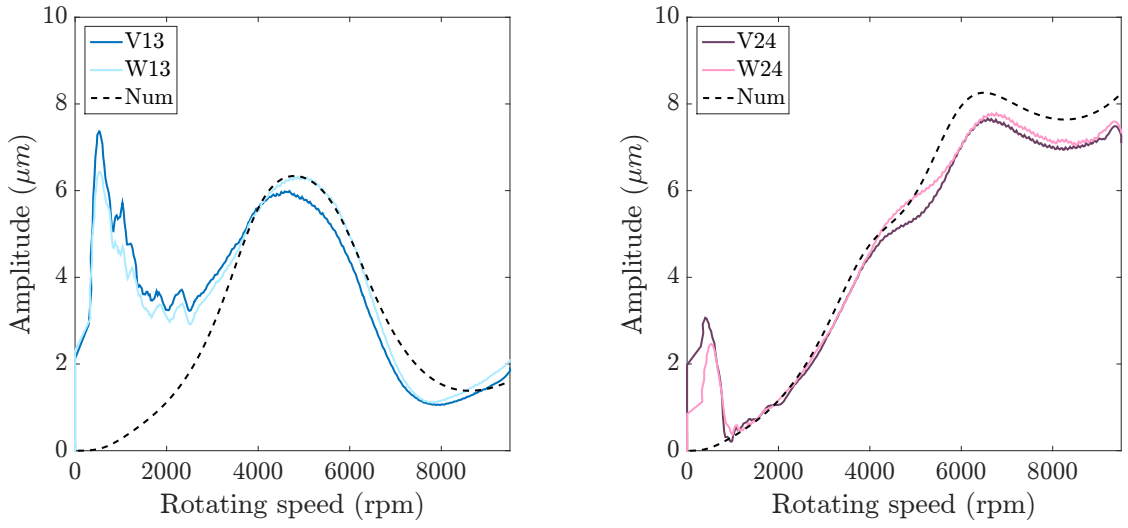


(a) DE side (b) NDE side

Figure 10: Predicted (dotted lines) vs measured mass unbalance response

DE side, are due to the electrical motor. Between 0 and 2 500 rpm, the motor was not able to produce a purely constant rotational speed. Investigations of base motion effects were then realised above 3 000 rpm.

### *4.2. Drop response*

The rotor is at rest and initially levitated by the AMBs. At 1 s, the AMBs are shut-down. The results of the predicted and measured drop responses are provided in Fig. 11.

The transient dynamics seems to be well described and the rotor displacements are comparable. The measurements demonstrate more damping during this phase and the predicted rebounds are larger at the

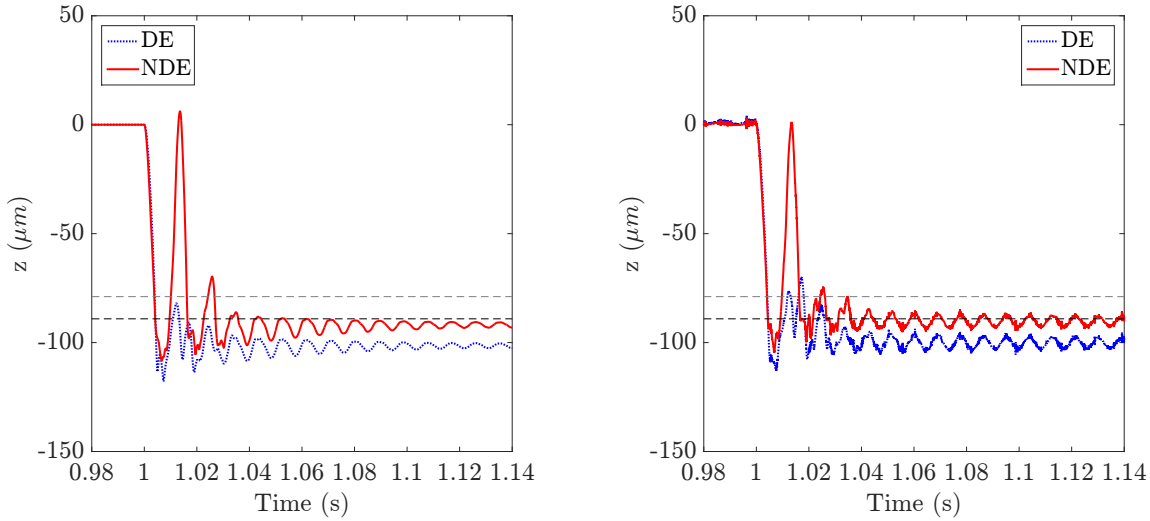


Figure 11: Predicted (a) vs measured (b) vertical rotor displacements (solid lines) and touchdown bearing clearances (dotted lines) - drop at rest

NDE side. It is noteworthy that this phase is affected especially by the vertical misalignments influencing the height of drop and the rotor trajectory. Once the transient passed, a low damped, small amplitude harmonic regime associated with the cylindrical mode of the coupled rotor-TDB system sets-up. This low damping could be due to the nonlinear stick-slip behaviour of ribbon dampers under harmonic loadings, as shown in Jarroux *et al.* [23]. Indeed, if the ribbon bumps remain in stuck position due to the too weak gravity loads, no slip transition occurs and quite no damping is generated while during the first rebounds, a slip state of the ribbon bumps generated by the larger drop loads could explain larger damping.

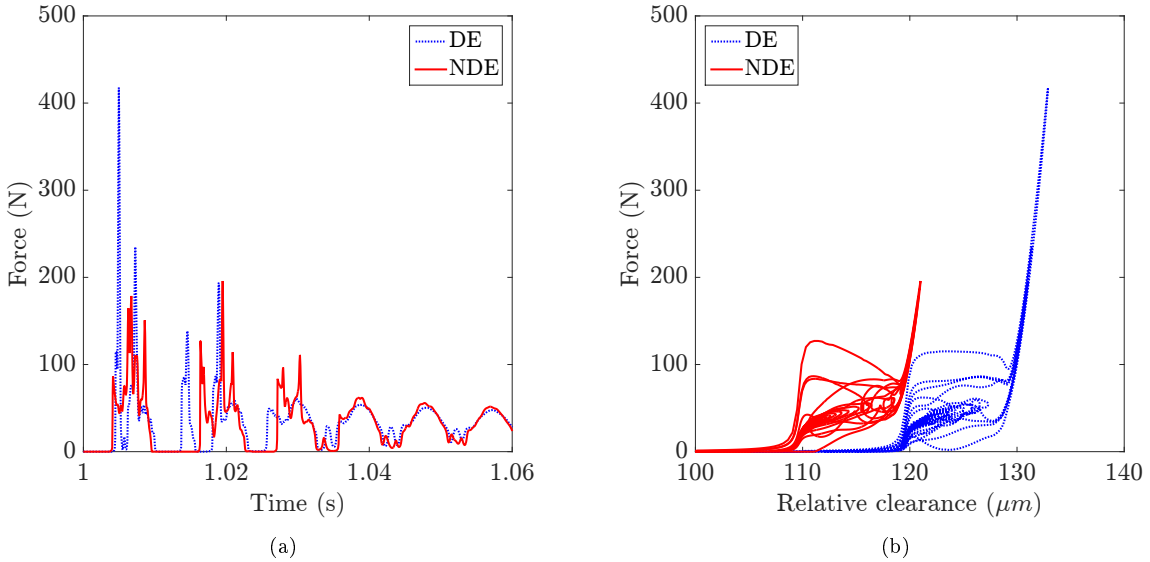


Figure 12: Predicted normal contact loads (a) and force-deflection loops (b) - drop at rest - [1-1.06]s

As the measured rotor drop dynamics is quite well described by the model, one can be confident on the predicted TDB contact loads which should be close to the real ones, and might overestimate them. The drop loads as well as the force-deflection loops are displayed in Fig. 12. The maximal loads are found at DE side with almost 400 N which is far lower from the estimated static load capacity of the TDBs. The peaks appearing during the first rebounds are related to the complete crushing of the ribbon damper, also revealed by the appearance of the tiny peaks in the force-deflection loops. The latter demonstrate the large damping provided by the ribbon during the first rebounds characterized by large areas. It is worth mentioning that when the rotor stabilizes at the bottom of its TDBs, the contact loads at both DE and NDE tend to 33 and 31 N respectively, which the sum is the rotor weight.

These preliminary tests show the effectiveness of the numerical model to reproduce quite accurately the measures for simple test cases.

## 5. Support motion investigations - Harmonic tests

The harmonic translation support motion was set to 20 Hz ranging from 0.1 to 1.1 G, see Fig. 13. The

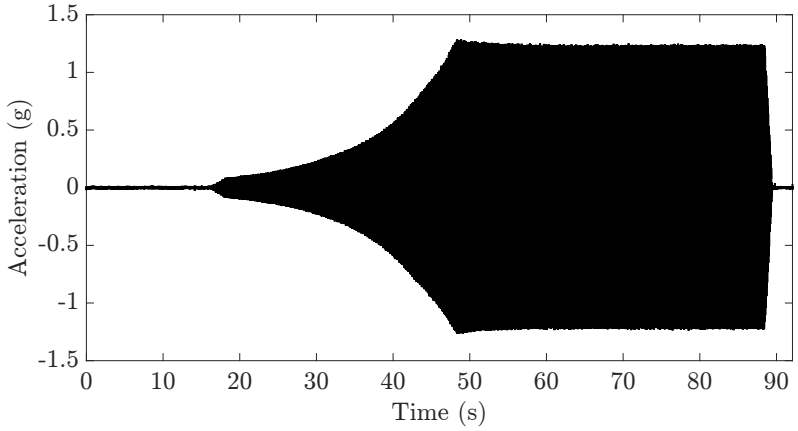


Figure 13: Measured base vertical acceleration (Zcube) - 0.1 to 1.1 G at 20 Hz

frequency was chosen according to the lowest AMB gain in order to easily trigger TDB contacts. Moreover, it is a representative frequency of earthquake whose energy is mainly comprised in the range [20-30] Hz, as explained by Matsushita *et al.* [28]. The targeted acceleration level was applied progressively, during almost 30 s, to limit overshoots and was then maintained for approximately 40 s to analyse potential onset of nonlinear dynamic regimes. The rotor speeds of rotation were set to 3 000, 6 000 and 9 500 rpm. For all the running tested, the same level of mass unbalance was applied: 32 g.mm at 0 degree that corresponds to four times the recommended mass unbalance by the API standards. These base motion tests have been carried out three times and it appeared that the observed phenomena considering the rotordynamics were repeatable each time. For this reason, only one test is further investigated hereafter.

The accelerations recorded on the shaker, Fig. 13, were implemented into the numerical model.

### *5.1. Overall dynamics*

This subsection is entirely treated using the case where the rotor is running at 6 000 rpm, the related observations being identical with respect to the 3 000 and 9 500 rpm cases. Fig. 14 displays the overall predicted and measured responses in vertical direction. After 10 s, the support motion starts and TDB contact occurred close to 35 s. The controller seems able to manage the mass unbalance forces combined with frame motions and TDB contacts. This is corroborated by the fact that once the shaker stops, the rotor quickly recovers its centred position. The measured and predicted rotor displacements are larger at the DE side because the DE controller gain is smaller but also because the centre of inertia is closer to this

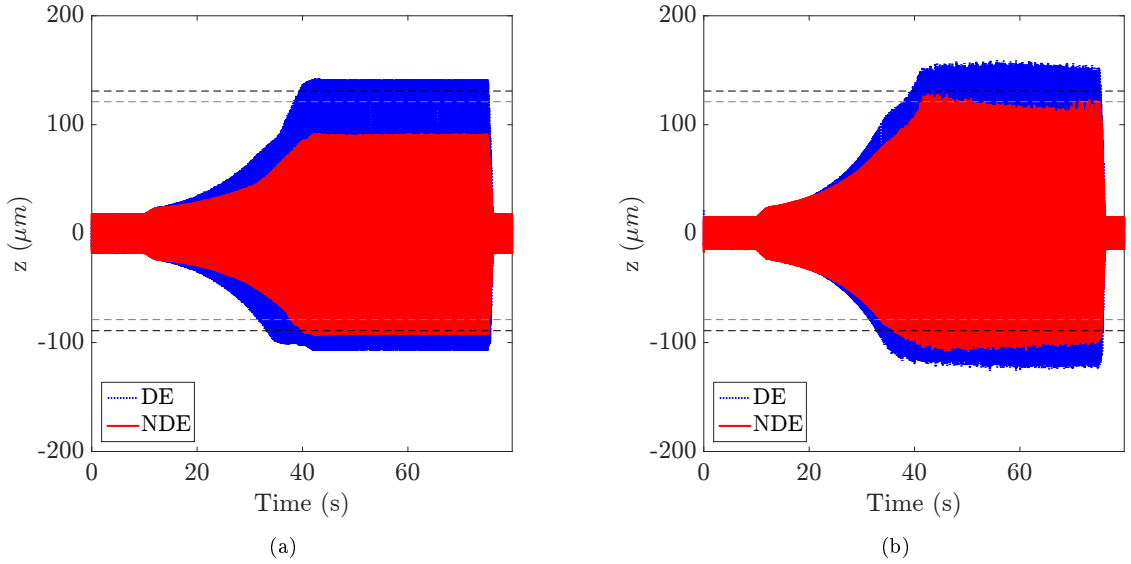


Figure 14: Predicted (a) vs measured (b) vertical rotor displacements (solid lines) and touchdown bearing clearances (dotted lines) - 6 000 rpm and 1.1 G at 20 Hz

bearing. The predicted normal contact loads are given in Fig. 15(a): they are small in comparison with those generated during a rotor drop at rest, see Fig. 12. The ribbon damper is not fully crushed: the ball bearing, comprising a much higher stiffness, is lightly loaded. The base motion overshoot effects is visible just after 40 s. TDBs are driven in rotations by the rubbing contacts, as displayed in Fig. 15(b). At the DE, the touchdown bearing reaches the rotor full speed while at the NDE side, it only reaches 4 000 rpm preceding by a maximum at 5 000 rpm associated with the overshoot.

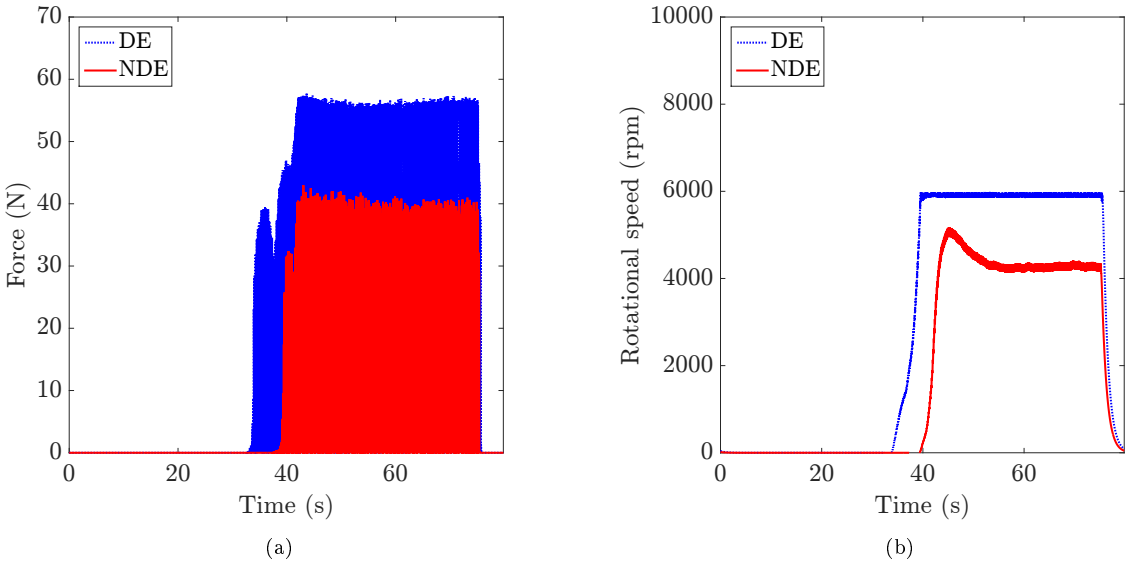


Figure 15: Predicted normal contact loads (a) and touchdown bearing speeds of rotation (b) - 6 000 rpm and 1.1 G at 20 Hz

More detailed rotordynamics are provided in Fig. 16 and 17 where a zoom on three base motions periods

is plotted both in vertical and horizontal directions. From a qualitative point of view, the predictions are close to measurements. The effects of contacts are visible in horizontal direction each five periods of rotating speed, which correspond to the base motion frequency. As expected, sliding friction forces are weak and this is due to small normal contact forces but also to a reduced relative sliding friction coefficient at the DE, resulting from the TDB full speed.

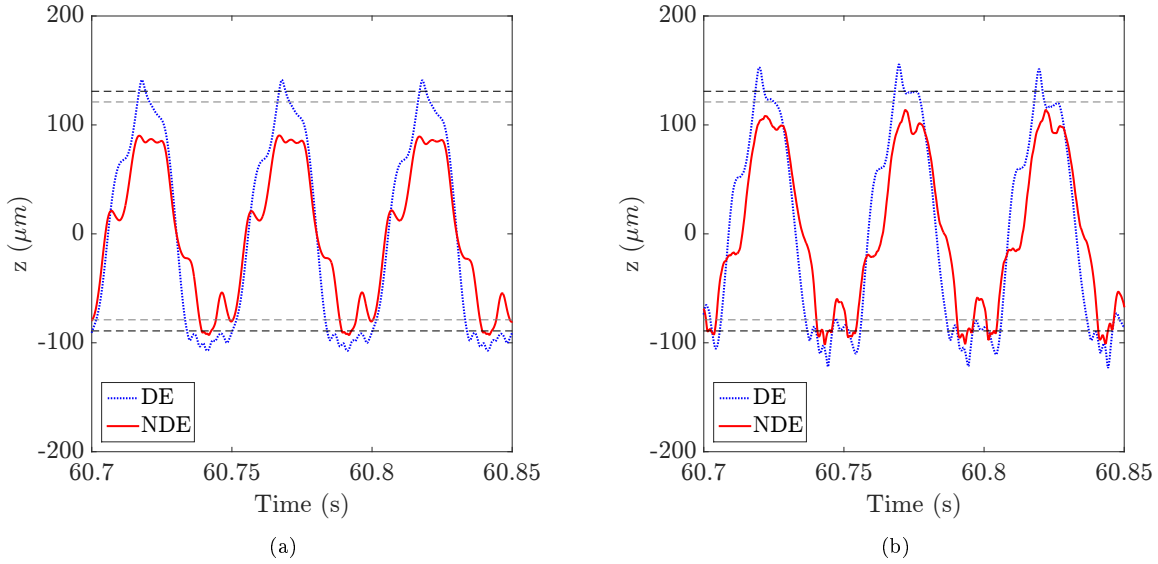


Figure 16: Predicted (a) vs measured (b) vertical rotor displacements (solid lines) and touchdown bearing clearances (dotted lines) - 6 000 rpm and 1.1 G at 20 Hz - zoom in the range [60.7-60.85]s

Predicted and measured top currents plots are given in Fig. 18 for all the action lines. The overall trends are similar. No amplifier saturation occurred and the control current remained in its nominal range. AMBs do not destabilize the rotor in both numerical and experimental results. The effects of contact generate high frequency current content, especially during the bottom rotor-TDB interactions. These effects are more noticeable in the measurements where the generated currents are amplified with respect to predictions, as if the controller gain was higher on these frequencies. This could be due to some differences between the numerical and experimental controller transfer functions, especially at the NDE side.

The Fig. 19 depicts the predicted TDB contact loads. It shows that the rotor oscillates due to a resonance effect of the rotor-TDB system. This could explain the high frequency content observed in the currents provided by the controller. It was difficult to obtain a value of that frequency since the TDB model has a nonlinear behaviour. According to the force-deflection relationship, the ribbon damper is not fully crushed, and the generated load remained limited.

Finally, it is shown that when the rotor exceeds the TDB clearance, loads are shared between AMBs and TDBs and the base motions are mainly counteracted by magnetic forces.

The spectral analysis gives further informations on the rotordynamics. In presence of contacts, nonlinear features such as sub-super harmonic responses or chaotic regimes may be highlighted. The time evolution of the NDE horizontal displacement frequency content is obtained through Short-Time Fourier Transform (STFT) and results are provided in Fig. 20 and 21, respectively.

The plots are composed of STFT and the average spectra, computed along the time axis. The predicted and measured results are qualitatively similar. The effects of contact are clearly highlighted, close to 30 s where a wide frequency bandwidth is excited, including the first three bending modes located close to 200, 580 and 1 140 Hz. Gyroscopic effects split these frequencies into forward and backward whirl modes: this is visible especially for the second and third bending modes. The level of response of these modes is, however, small. The full spectrum, usually computed to determine whether the rotor orbit motion frequency

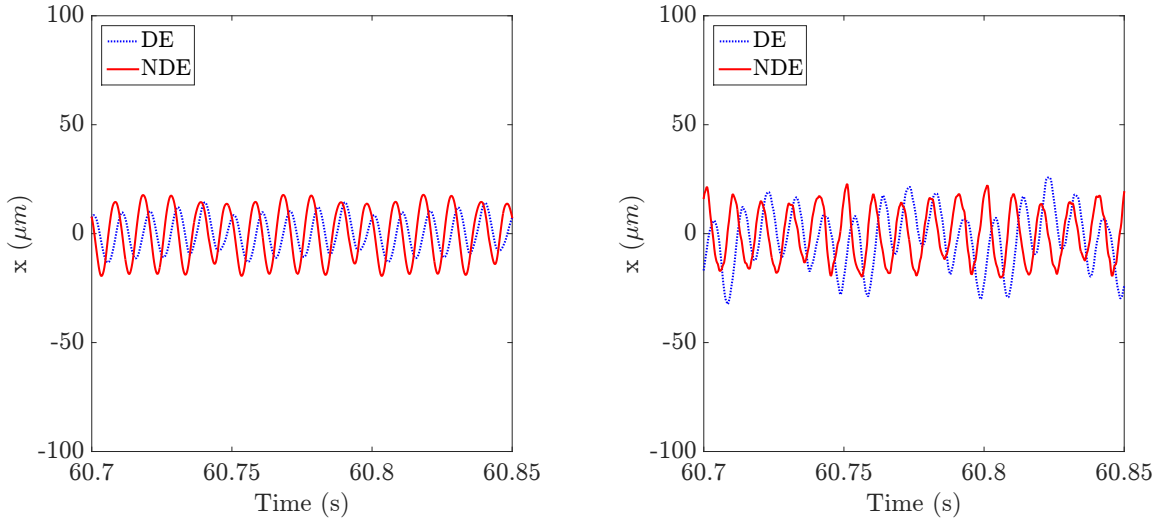


Figure 17: Predicted (a) vs measured (b) horizontal rotor displacements (solid lines) - 6 000 rpm and 1.1 G at 20 Hz - zoom in the range [60.7-60.85]s

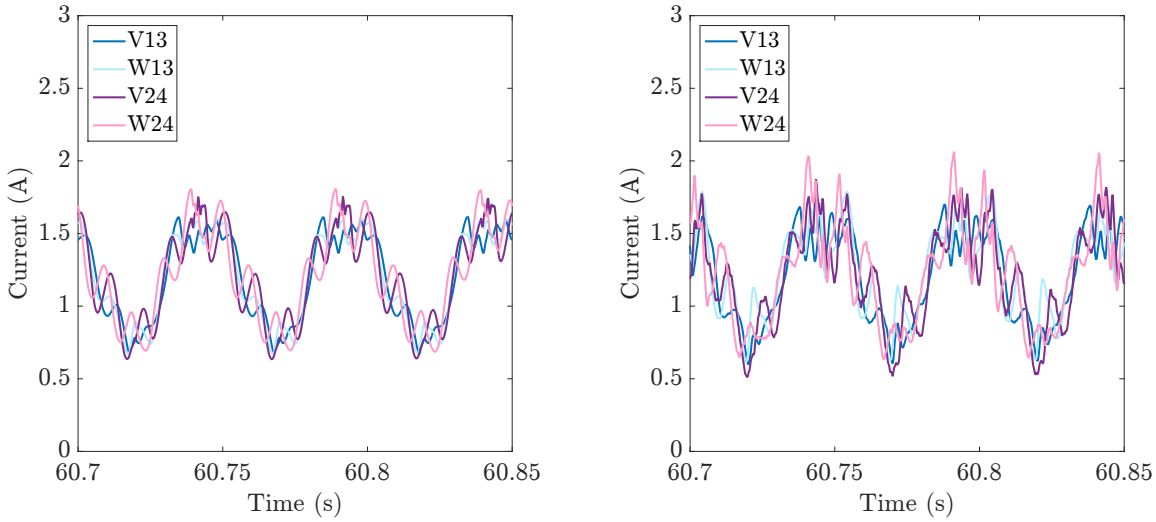


Figure 18: Predicted (a) vs measured (b) top currents - 6000 rpm and 1.1 G at 20 Hz - zoom in the range [60.7-60.85]s

components are forward or backward, was not employed here since no particular backward whirl components were observed.

### *5.2. Orbital responses*

Orbit plots provide insights onto rotordynamics and permit analysing the combined effects of mass unbalance forces, base motion loads with TDB interactions. Once the requested support acceleration of 1.1 G is reached, this combination can be further analysed.

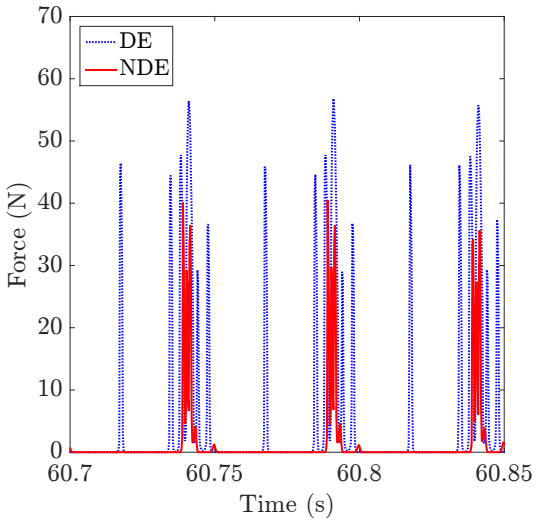


Figure 19: Predicted normal contact loads - 6 000 rpm and 1.1 G at 20 Hz - zoom in the range [60.7-60.85]s

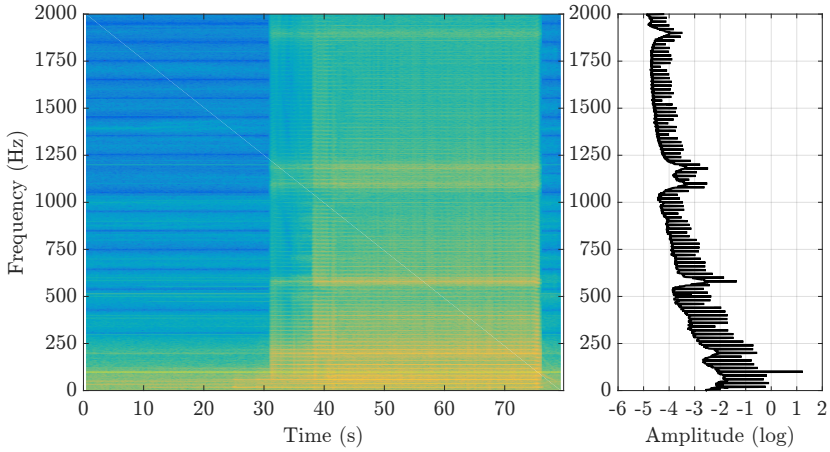


Figure 20: Predicted NDE STFT and average spectrum in horizontal direction - 6 000 rpm and 1.1 G at 20 Hz

The predicted and measured orbits of the rotor subjected to 1.1 G base acceleration are respectively plotted in Fig. 22, 23 and 24 running at 3 000, 6 000 and 9 500 rpm. These plots are obtained based on ten base motion periods.

The rotor orbits are flattened at the bottom and the top by the TDB interactions and specific periodicities can be observed.

Driot *et al.* [6] showed that when the ratio $n$ between the base rotation frequency $\omega$ and the speed of rotation $\Omega$ was a rational number, periodic orbits were found and while when it was a ordinary one, they were quasi-periodic. This conclusion may be extended for the translation case since typical combinations of foundation motions and mass unbalance forces are exhibited. In this case, the TDB contacts do not change these periodicities.

This can be demonstrated by the Eq. (23).

$$\omega = \frac{\beta}{\chi}\Omega = n\Omega \tag{23}$$

where $\beta$ and $\chi$ are integers. When $\Omega$ equals 3 000 rpm and 6 000 rpm, orbits are periodic and the ratio $n$

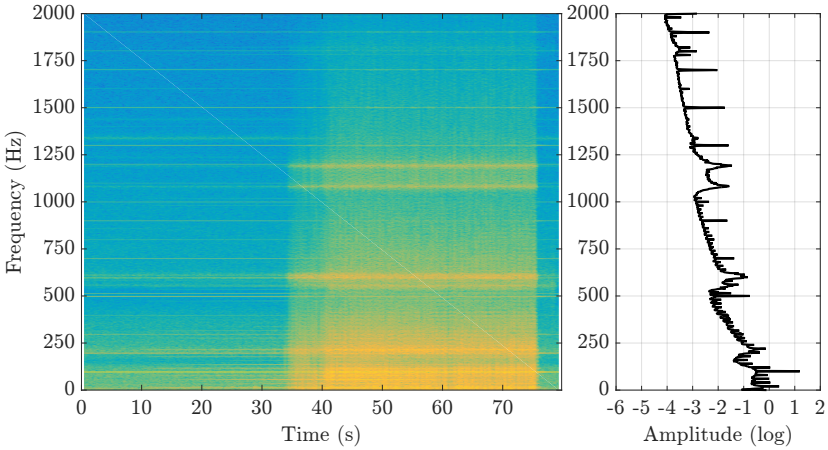


Figure 21: Measured NDE STFT and average spectrum in horizontal direction - 6 000 rpm and 1.1 G at 20 Hz

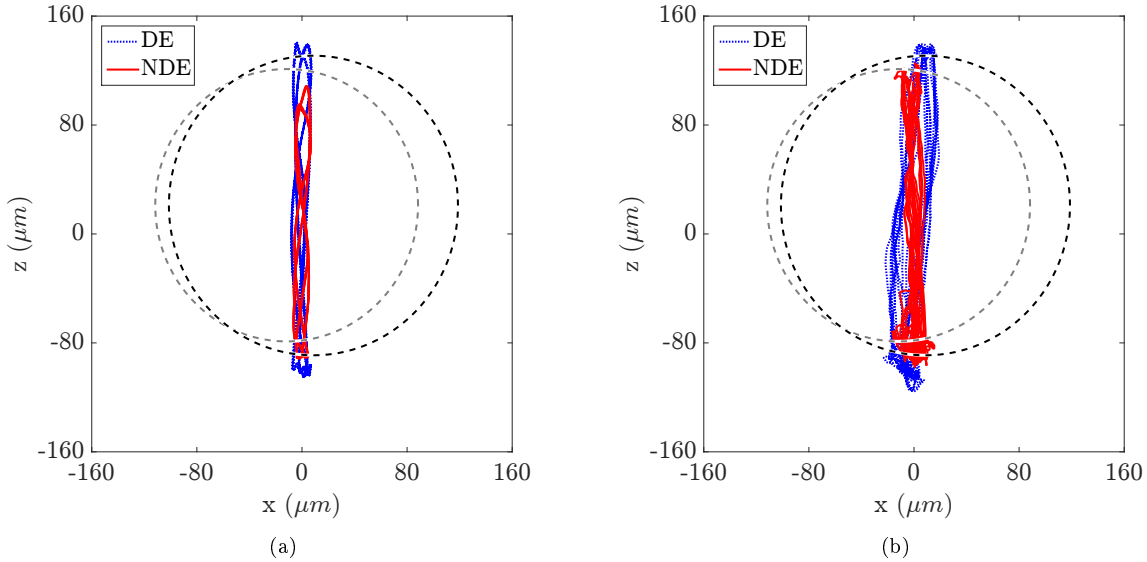


Figure 22: Predicted (a) vs measured (b) rotor orbits (solid lines) and touchdown bearing clearances (dotted lines) - 3 000 rpm and 1.1 G at 20 Hz

is a rational whereas when $\Omega$ equals 9 500 rpm, orbits are quasi-periodic and $n$ becomes an ordinary. Table 4 summarizes these results.

Table 4: Rotor orbit periodicities

| | **3 000 rpm** | **6 000 rpm** | **9 500 rpm** |
|---|---|---|---|
| $\beta$ | 2 | 1 | 20 |
| $\chi$ | 5 | 5 | 158 |
| n | rational | rational | ordinary |
| Orbit type | periodic | periodic | quasi-periodic |

Orbit plots exhibit mainly forward whirl indicating low sliding friction effects. As previously explained,

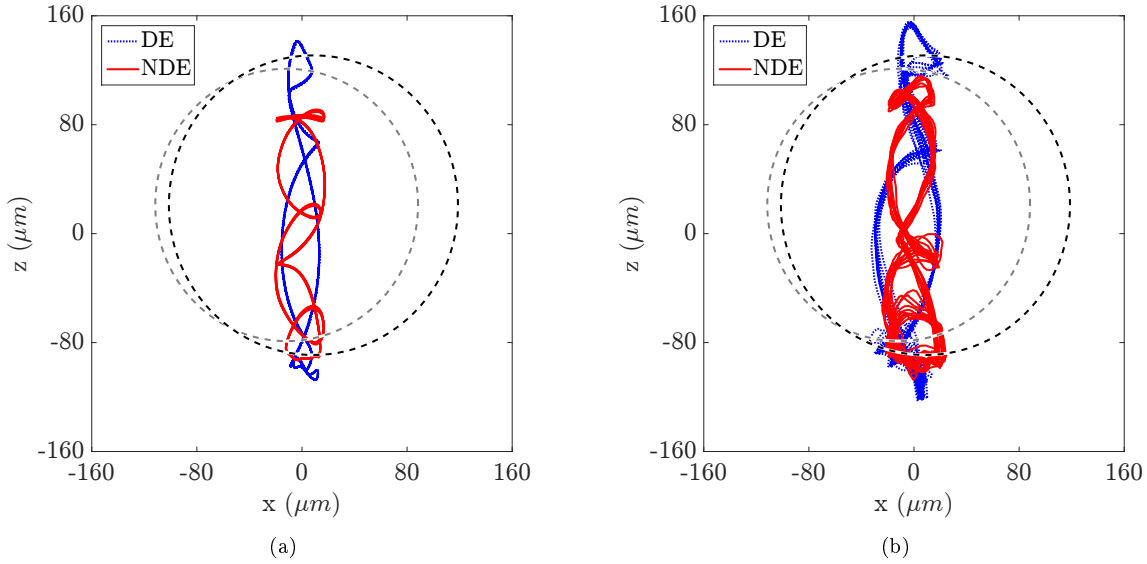


Figure 23: Predicted (a) vs measured (b) rotor orbits (solid lines) and touchdown bearing clearances (dotted lines) - 6 000 rpm and 1.1 G at 20 Hz

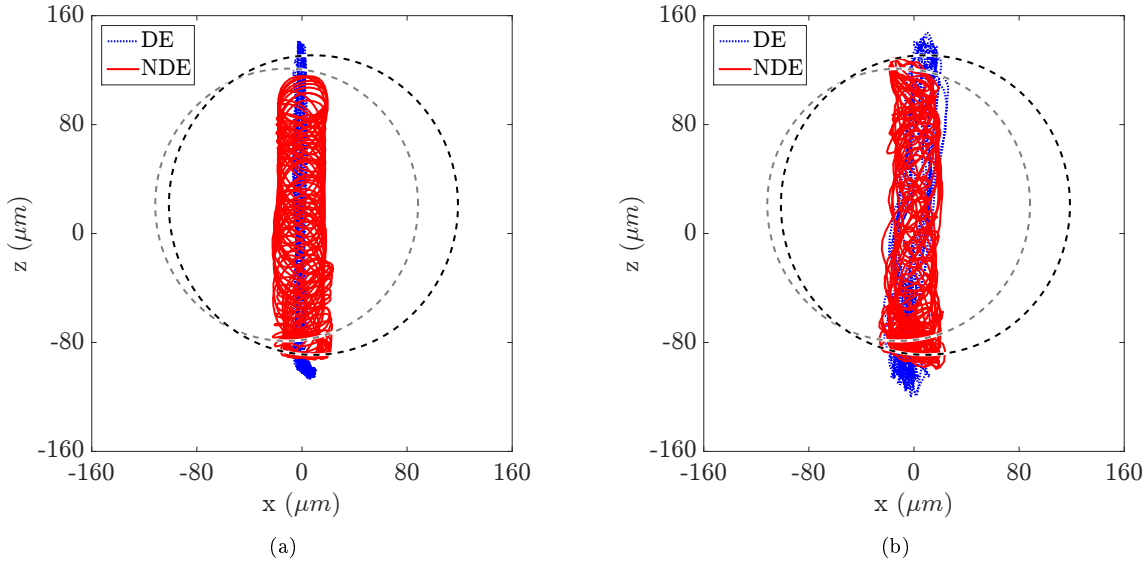


Figure 24: Predicted (a) vs measured (b) rotor orbits (solid lines) and touchdown bearing clearances (dotted lines) - 9 500 rpm and 1.1 G at 20 Hz

this could be the consequence of weak normal contact loads, since base motions are mainly counteracted by AMBs, but also of weak rotor-TDB relative sliding velocities. Indeed, as the latter are driven in rotation by the friction forces produced by intermittent contacts, they quickly reach the rotor speed of rotation.

## 6. Support motion investigations - Impulse tests

The impulse tests were also carried out in vertical direction. The shock lasted 0.02 s (50 Hz) and increased from 0.5 to the set value of 3.1 G. Once the acceleration set level reached, ten shocks were repeated each second as shown in Fig. 25. The applied mass unbalance was the same according to harmonic tests, 32 g.mm at 0 degree. The rotor speed of rotation was set to 9 500 rpm. As for the harmonic case, these base motion tests have been carried out three times and it appeared that the observed phenomena considering the rotordynamics were repeatable each time. For this reason, only one test is further investigated hereafter.

The accelerations recorded on the shaker, see Fig. 25, were implemented into the numerical model.

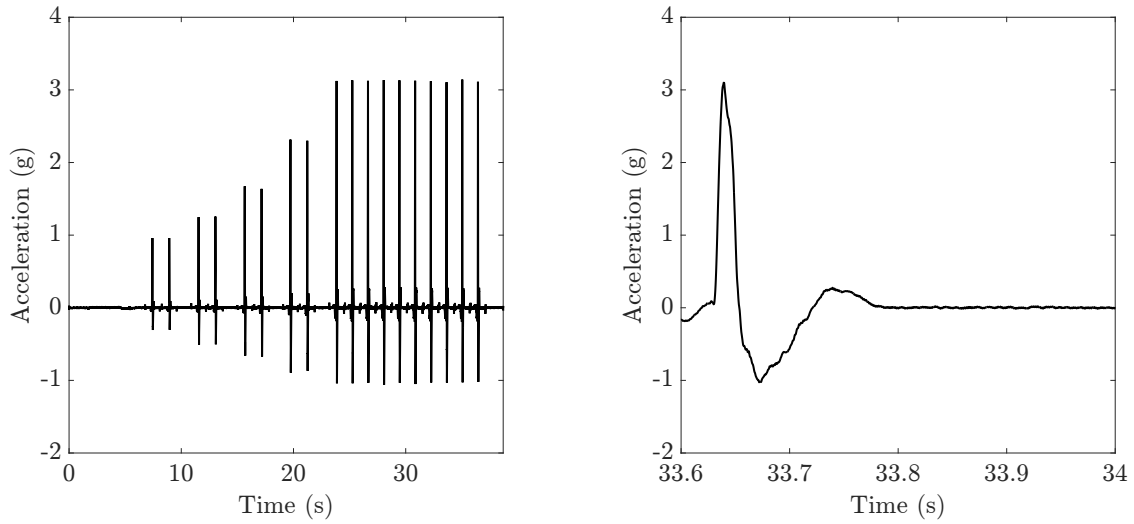


(a) Complete impulse test

(b) Zoom on one shock

Figure 25: Measured repeated shocks of the base (Zcube) - 3.1 G at 50 Hz

### *6.1. Overall dynamics*

From an overall point of view, the rotor response predictions and measurements in vertical direction look in agreement, as displayed in Fig. 26.

The measured displacements are larger than the predicted, and this is visible especially during the first shocks. No dangerous friction-induced vibration regimes are triggered and the rotor is quickly centred after each shock without generating established instabilities. As for harmonic cases, the currents remain in reasonable range (less than 2.2 A) for both measures and predictions up to 3.1 G.

The predicted normal contact loads are given in Fig. 27(a). The maximum values reach almost 600 N and 320 N at DE and NDE, respectively, and are related to the maximal acceleration level. During contact, the TDBs are driven in rotation but never reach the rotor full speed as shown in Fig. 27(b). The rotor-TDB relative sliding velocity is then always large and the dynamic friction coefficient is expressed.

Figure 28 displays results during one impulse. The acceleration profile is also plotted in green: the related values have no physical meanings, the maximum value being 3.1 G. Numerical and experimental results are close during the first phase of the shock, related to the maximum acceleration level, between the point 1 and 2 on the Fig. 28. Then, the measured rotor rebounds show that for one base shock, three successive contacts are generated while two are predicted.

### *6.2. Sliding friction effects*

The TDB contact loads are rather large with respect to the drop or the harmonic response. Moreover, the sliding friction effects are more expected to occur since TDB never reach the rotor full speed. This

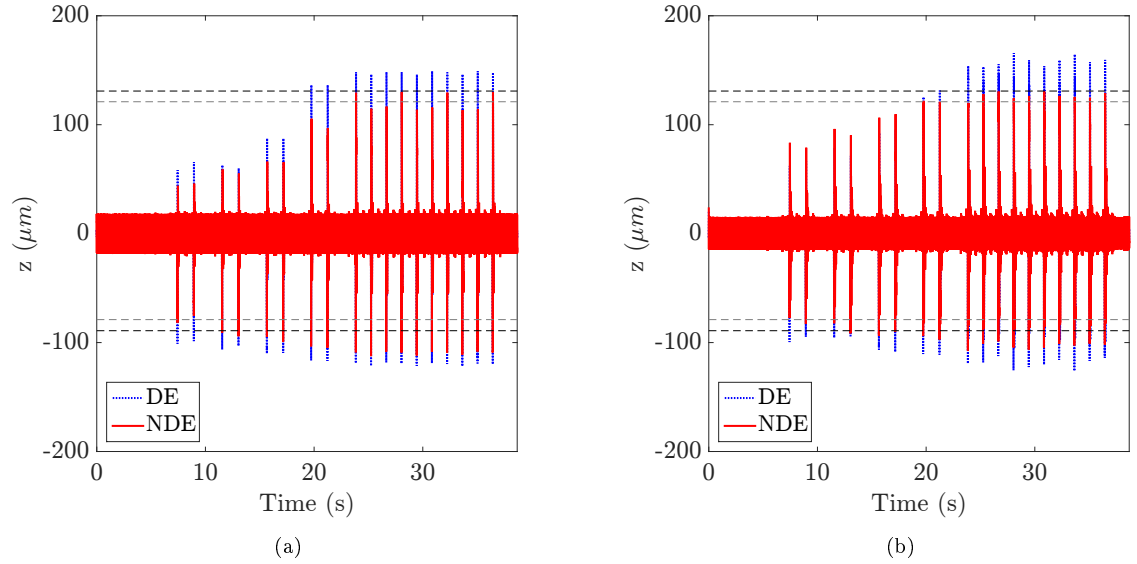


Figure 26: Predicted (a) vs measured (b) vertical rotor displacements (solid lines) and touchdown bearing clearances (dotted lines) - 9 500 rpm and 3.1 G at 50 Hz

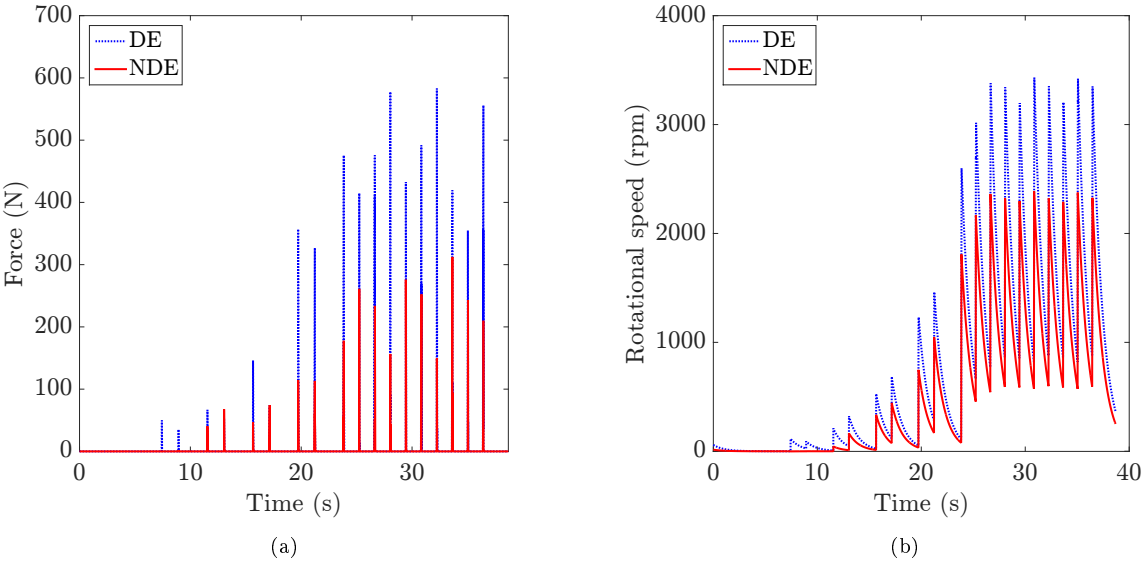


Figure 27: Predicted normal contact loads (a) and touchdown bearings speed of rotation (b) - 9 500 rpm and 3.1 G at 50 Hz

subsection is devoted to the analysis of the tangential friction force effects on the rotordynamics throughout the duration of the first contact, located at the bottom of the TDBs. The related range in time domain are set between the instants 1 and 2, in Fig. 28. The predicted and measured orbits on that particular range are given in Fig. 29.

The initial forward whirl response, indicated by the black arrow, is induced by the mass unbalance forces. As observed in the time domain, the first contact is described well by the numerical model, at both DE and NDE sides, in terms of height and direction of rebound. The blue and red arrows indicate the instantaneous rotor whirl directions at the DE and NDE sides, respectively. Sliding friction effects are clearly visible in

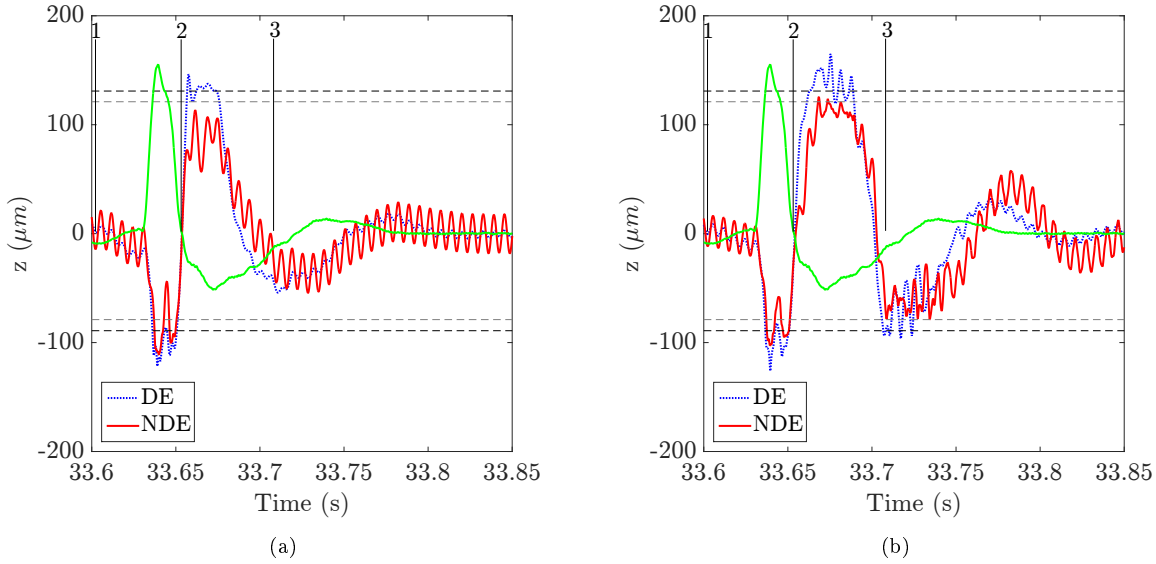


Figure 28: Predicted (a) vs measured (b) vertical rotor displacements (solid lines), touchdown bearing clearances (dotted lines) and acceleration profile (green lines) - 9 500 rpm and 3.1 G at 50 Hz - zoom on one shock

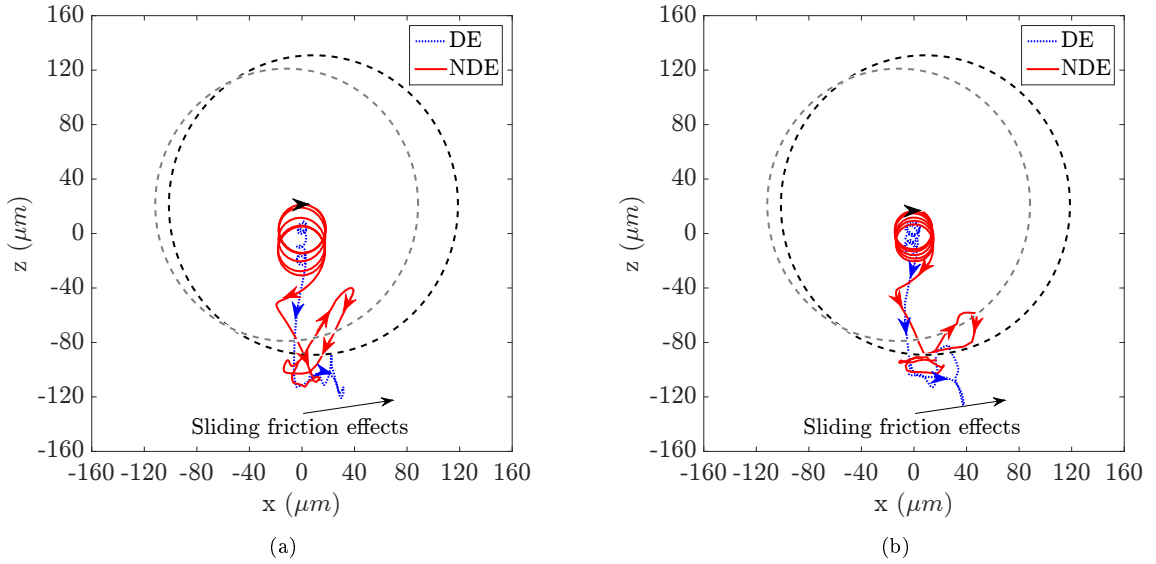


Figure 29: Predicted (a) vs measured (b) rotor orbits - 9 500 rpm and 3.1 G at 50 Hz - between the instants 1 and 2 in Figure 28

Fig. 29 since orbit has backward whirl during the contact.

### *6.3. Fleeting instabilities*

This subsection provides further insights into particular phenomena observed during impulse tests. It is shown, in Fig. 28, that the second measured rotor rebound, located at the top of TDBs, seemed more violent than the predicted one while the normal contact loads should logically be smaller. The orbit responses between the instants 1 and 3 are given in Fig. 30 with a measured "fleeting event" during the top contact.

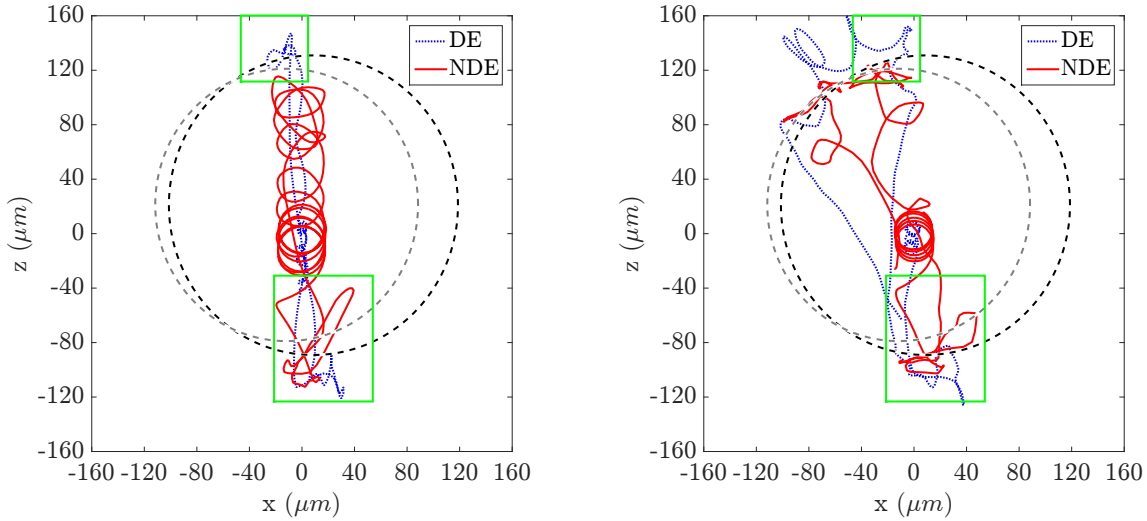


(a) (b)

Figure 30: Predicted (a) vs measured (b) rotor orbits - 9 500 rpm and 3.1 G at 50 Hz - between the instants 1 and 3 in Fig. 28

To understand this phenomenon, each of the bottom and top contacts (green rectangle) are analysed by means of orbit plots superimposed with the AMB force vectors. Indeed, the predicted and measured coil currents permit the computation of the applied magnetic forces, given at each time step by blue and purple arrows for the DE and NDE AMBs respectively. The rotor trajectory, or instantaneous whirl, is represented by black arrows, numbered in chronological order, from 1 to 5 and specifically at the DE side since trends are identical at the NDE side. This permits analysing the capacity of AMB to counteract TDB forces throughout the duration of contact. The predicted and measured bottom contacts are depicted in Fig. 31. As previously shown, the rotor trajectory is qualitatively well described by the model. In both measures and predictions, the magnetic forces counteract the effects of base motion and TDB contact. After the rebound, the rotor is pushed to recover its centred position.

A zoom on the top contact is provided in Fig. 32. It seems that during a short period, the measured magnetic forces at DE side push the rotor in backward direction between the arrows 3 and 4, but not in the predictions. This could be due to negative damping provided by the experimental AMB transfer function or to the controller delay to apply the instruction. Obviously, tangential forces induced by friction contributes also to this backward whirl motion. However, the predicted contact loads, especially the tangential ones, are supposed to be small during the top contact.

Just after this event, the rotor is quickly recentred by the AMBs and no established instabilities are triggered.

## 7. Outcomes and discussions

The test configurations were chosen to be representative of high speed industrial turbomachinery where the rotor has no bending modes in the operating speed range and the PID controller was tuned for conventional rotordynamics. The numerical and experimental investigations for harmonic and impulse tests in vertical direction were conducted:

- Considering harmonic tests, TDB contact generates the rotor displacements flattening and rich frequency responses comprising many superharmonics of the fundamental base motion frequency and modal content. The restoring magnetic forces generated by actuators remain in an acceptable linear range. No amplifier saturations were noticed. The rotor-TDB coupled modes are excited throughout

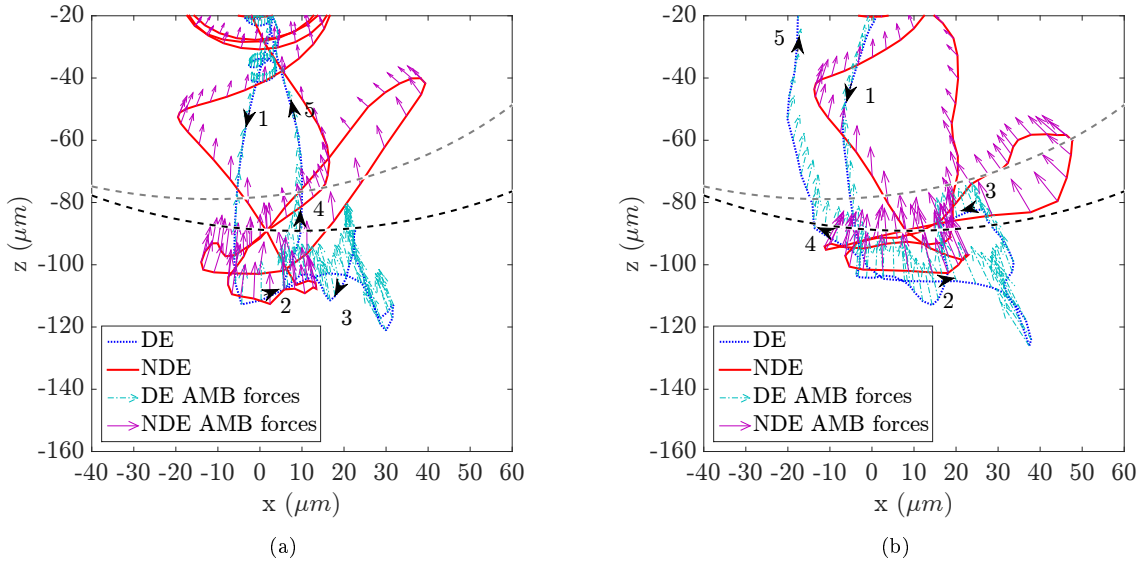


(a) (b)

Figure 31: Predicted (a) vs measured (b) rotor orbits and AMB forces during the bottom TDB contact - 9 500 rpm and 3.1 G at 50 Hz - between the instants 1 and 2 in Fig. 28

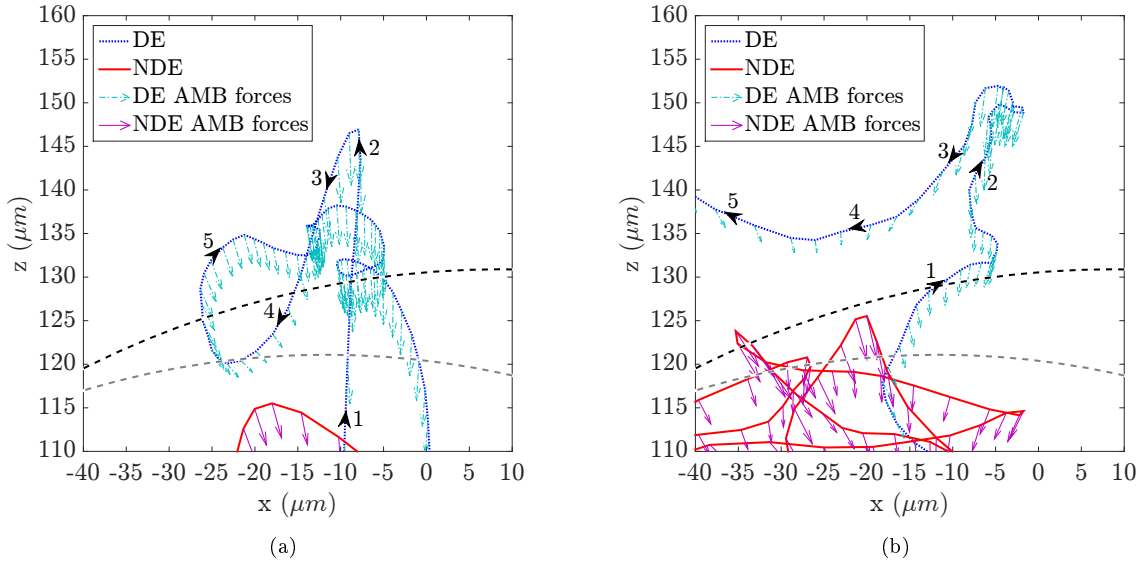


(a) (b)

Figure 32: Predicted (a) vs measured (b) rotor orbits and AMB forces during the top TDB contact - 9 500 rpm and 3.1 G at 50 Hz - between the instants 1 and 2 in Fig. 28

the duration of each contact. Even if the PID controller was tuned without considering these particular frequencies, the rotor-AMB controller remains globally stable in both numerical and experimental tests. The rubbing contacts did not triggered dry whip instabilities in both experimental and numerical results. It seems that the TDBs are driven in rotation reaching the rotor rotational speed during harmonic tests: tangential friction effects are limited. Moreover, the acceleration level did not generate large contact loads.

- Considering impulse tests, the sliding friction effects are more visible. On the one hand, because the

acceleration levels tested were higher and on the other hand, because the TDBs are not driven in rotation up to the rotor speed. The sliding friction was then higher than for harmonic cases. At the bottom contact, short periods of backward whirl were exhibited both in predictions and measures with similar amplitude. The rotor was then quickly recentred. At the top contact, some fleeting instabilities were recorded experimentally. The latter are most likely to be triggered by AMBs since during a short period, AMBs pushed the rotor in the sens of its trajectory. These instabilities failed to settle and the rotor was always quickly recentred just after.

- For all these analyses, no AMB nonlinearity was exhibited, in both predictions and measures, whether amplifier saturation or strong magnetic force nonlinearity. This is mainly due to the fact that TDB contacts prevent actuator nonlinearities emergences. It should be mentioned that the TDB over AMB clearances ratio is close to 0.25 which is smaller than industrial values, closer to 0.5, making the nonlinearities of the actuator restoring forces more relevant.

Phenomena associated with rotor-TDB interactions are sensitive to contact parameters such as clearance, misalignments, damping and stiffness, sliding friction, boundary conditions, etc. On the other hand, rotor-AMB systems are also sensitive to the electromagnetic forces driven by the controller. The combination of both these phenomena is complex and several discrepancies were noticed when comparing predicted and measured results:

- The fleeting events observed during impulse tests were not predicted by the model. A slight difference between the numerical and the experimental AMB transfer function, not plotted in this article, was noticed. The identification procedure carried-out revealed that the amplifier was the most probable source of discrepancies.

- The measured rotor-TDB clearance was not exactly the provided one. Several assumptions can explain these differences: manufacturing issues, the uncertainties of TDB internal clearance and ribbon parameters, the ribbon elastoplastic behaviour (dry-friction during the crush).

- Measured orbits at both DE and NDE sides are not perfectly vertical and are symmetrically tilted with respect to the vertical axis. This is probably due to the assembly, introducing a twist between the DE and NDE AMBs. Therefore, the base motion in vertical direction appears to be slightly inclined in the DE and NDE AMB sensors.

## 8. Conclusions

The aim of this research work was to provide further insights into the understanding of the dynamic behaviour of embedded rotor-AMB systems and to carried out an experimental validation of the proposed model. The effects of base motions, involving TDB interactions, on the system dynamics and on AMBs were of particular interest.

The developed numerical model permits performing nonlinear and transient simulations in order to understand phenomena and to have a reliable tool enabling the optimization of the system performance. It comprises an on-board rotor, active magnetic bearings (augmented PID controller and nonlinear actuator forces) and touchdown bearings (contact law and rotational dynamics). A lab-scale test rig, designed to be representative of industrial turbomachinery, was employed to perform harmonic and impulse testings. The control strategy was not specifically tuned to withstand bases excitations.

Harmonic base excitation demonstrate periodic or quasi-periodic orbits depending on the ratio between the base motion and the speed of rotation. Rotor orbit shapes are flattened by TDB interactions. Forward whirls were exhibited and no dry whip instabilities were noticed. Considering impulse excitations, short periods of backward whirl induced by TDB rubbing contacts were observed. The restoring magnetic forces generated by actuators remained in an acceptable linear range and no amplifier saturations were exhibited. Even if the PID controller was tuned without considering this particular excitation, it remained mostly stable in both numerical and experimental tests.

The model was able to reproduce the overall dynamics and the main observed phenomena which provides confidence considering the prediction of the dynamic behaviour of on-board industrial turbomachinery. In particular, this model will be use to conduct further investigations regarding the influence of TDBs, AMBs and mass unbalance parameters on the rotordynamics. The aim will be to extend the understanding of phenomena, to analyse the system sensitivity to parameter changes and to provide efficient design solutions to avoid dangerous dynamics, such as dry-whip.

## 9. Acknowledgement

This work was supported by the ANRT (French National Research and Technology Agency), CIFRE [grant number 2013/1376]. The experimentations were carried out with the 6-axis shaker of Equipex PHARE 10-EQPX-0043 of the ANR (French National Research Agency) funded by the PIA (Programme d'Investissements d'Avenir).

## References

[1] B. Samali, K. Kim, J. Yang, Random vibration of rotating machines under earthquake excitations, Journal of Engineering Mechanics 112 (6) (1986) 550–565.

[2] M. Ghafory-Ashtiany, M. P. Singh, Structural response for six correlated earthquake components, Earthquake Engineering & Structural Dynamics 14 (1) (1986) 103–119.

[3] Y. Hori, T. Kato, Earthquake-induced instability of a rotor supported by oil film bearings, Journal of Vibration and Acoustics 112 (2) (1990) 160–165.

[4] L. E. Suarez, M. P. Singh, M. S. Rohanimanesh, Seismic response of rotating machines, Earthquake Engineering & Structural Dynamics 21 (1) (1992) 21–36.

[5] A. S. Lee, B. O. Kim, Y. C. Kim, A finite element transient response analysis method of a rotor-bearing system to base shock excitations using the state-space newmark scheme and comparisons with experiments, Journal of Sound and Vibration 297 (3-5) (2006) 595–615.

[6] N. Driot, C. H. Lamarque, A. Berlioz, Theoretical and experimental analysis of a base-excited rotor, Journal of Computational and Nonlinear Dynamics 1 (2006) 257–263.

[7] M. Duchemin, A. Berlioz, G. Ferraris, Dynamic behavior and stability of a rotor under base excitation, Journal of Vibration and Acoustics 128 (5) (2006) 576–585.

[8] M. Dakel, S. Baguet, R. Dufour, Steady-state dynamic behavior of an on-board rotor under combined base motions, Journal of Vibration and Control 20 (15) (2014) 2254–2287.

[9] Q. Han, F. Chu, Parametric instability of flexible rotor-bearing system under time-periodic base angular motions, Applied Mathematical Modelling 39 (15) (2015) 4511–4522.

[10] Y. Briend, M. Dakel, E. Chatelet, M.-A. Andrianoely, R. Dufour, S. Baudin, Effect of multi-frequency parametric excitations on the dynamics of on-board rotor-bearing systems, Mechanism and Machine Theory 145 (2020) 103660.

[11] A. S. Das, J. K. Dutt, K. Ray, Active vibration control of unbalanced flexible rotor-shaft systems parametrically excited due to base motion, Applied Mathematical Modelling 34 (9) (2010) 2353–2369.

[12] T. Soni, A. Das, J. Dutt, Active vibration control of ship mounted flexible rotor-shaft-bearing system during seakeeping, Journal of Sound and Vibration 467 (2020) 115046.

[13] R. Bouziani, N. Ouelaa, Simulation of the dynamic behavior of a rotor subject to base motion under variable rotational speed, Mechanics & Industry.

[14] F. M. A. El-Saeidy, F. Sticher, Dynamics of a rigid rotor linear/nonlinear bearings system subject to rotating unbalance and base excitations, Journal of Vibration and Control 16 (3) (2010) 403–438.

[15] M. Dakel, S. Baguet, R. Dufour, Nonlinear dynamics of a support-excited flexible rotor with hydrodynamic journal bearings, Journal of Sound and Vibration 333 (10) (2014) 2774–2799.

[16] G. Schweitzer, E. H. Maslen, Magnetic Bearings, Theory, Design, and Application to Rotating Machinery, Springer-Verlag, 2009.

[17] A. Gelin, J. M. Pugnet, J. Der Hagopian, Dynamic behavior of flexible rotors with active magnetic bearings on safety auxiliary bearings, in: Proceedings of Third International Conference on Rotordynamics, Lyon, France, 1990, pp. 503–508.

[18] J. Schmied, J. C. Pradetto, Behaviour of a one ton rotor being dropped into auxiliary bearings, in: 3rd International Symposium on Magnetic Bearing, 1992, pp. 145–156.

[19] E. H. Maslen, L. E. Barrett, Rotor whirl in compliant auxiliary bearings, Journal of Vibration and Control 2 (2) (1996) 145–159.

[20] M. O. T. Cole, P. S. Keogh, C. R. Burrows, The dynamic behavior of a rolling element auxiliary bearing following rotor impact, Journal of Tribology 124 (2) (2001) 406–413.

[21] G. Sun, A. B. Palazzolo, A. Provenza, G. Montague, Detailed ball bearing model for magnetic suspension auxiliary service, Journal of Sound and Vibration 269 (3-5) (2004) 933–963.

[22] A. Kärkkäinen, J. Sopanen, A. Mikkola, Dynamic simulation of a flexible rotor during drop on retainer bearings, Journal of Sound and Vibration 306 (3-5) (2007) 601–617.

[23] C. Jarroux, R. Dufour, J. Mahfoud, B. Defoy, T. Alban, A. Delgado, Touchdown bearing models for rotor-amb systems, Journal of Sound and Vibration 440 (2019) 51 – 69.
[24] C. Yu, Y. Sun, H. Wang, W. Shan, Y. Chen, R. Qiu, Dynamic analysis of magnetic bearing rotor dropping on radial and axial integrated auxiliary bearing, Mechanism and Machine Theory 140 (2019) 622 – 640.
[25] N. Neisi, J. Heikkinen, T. Sillanpää, T. Hartikainen, J. Sopanen, Performance evaluation of touchdown bearing using model-based approach, Nonlinear Dynamics 101 (1) (2020) 211 – 232.
[26] X. Kang, A. Palazzolo, W. Zhong, Auxiliary bearing squeeze film dampers for magnetic bearing supported rotors, Tribology International 146 (2020) 106181.
[27] Y. Murai, K. Watanabe, Y. Kanemitsu, Seismic test on turbo-molecular pumps levitated by active magnetic bearing, in: G. Schweitzer (Ed.), Magnetic Bearings: Proceedings of the First International Symposium, ETH Zurich, Switzerland, June 6-8, 1988, Springer Berlin Heidelberg, Berlin, Heidelberg, 1989, pp. 303–310.
[28] O. Matsushita, T. Imashima, Y. Hisanaga, H. Okubo, Aseismic vibration control of flexible rotors using active magnetic bearing, Journal of Vibration and Acoustics 124 (1) (2001) 49–57.
[29] Y. Suzuki, Acceleration feedforward control for active magnetic bearing systems excited by ground motion, IEE Proceedings - Control Theory and Applications 145 (2) (1998) 113–118.
[30] S. Marx, C. Nataraj, Suppression of base excitation of rotors on magnetic bearings, International Journal of Rotating Machinery 2007 (2007) 10.
[31] M. S. Kang, W. H. Yoon, Acceleration feedforward control in active magnetic bearing system subject to base motion by filtered-x lms algorithm, IEEE Transactions on Control Systems Technology 14 (1) (2006) 134–140.
[32] H. S. Kim, H. Y. Kim, C. W. Lee, T. H. Kang, Stabilization of active magnetic bearing system subject to base motion, in: ASME 2003 International Design Engineering Technical Conferences and Computers and Information in Engineering Conference, no. 37033, 2003, pp. 2007–2013.
[33] M. S. Kang, J. Lyou, J. K. Lee, Sliding mode control for an active magnetic bearing system subject to base motion, Mechatronics 20 (1) (2010) 171–178.
[34] M. O. T. Cole, P. S. Keogh, C. R. Burrows, Vibration control of a flexible rotor/magnetic bearing system subject to direct forcing and base motion disturbances, Proceedings of the Institution of Mechanical Engineers, Part C: Journal of Mechanical Engineering Science 212 (7) (1998) 535–546.
[35] P. S. Keogh, M. Necip, S. Clifford, R. Burrows, S. Prabhakar, Wavelet based adaptation of h-infinity control in flexible rotor/magnetic bearing systems, in: 7th IFToMM International Conference on Rotor Dynamics, Vienna, Austria, 2006.
[36] Y. Maruyama, T. Mizuno, M. Takasaki, Y. Ishino, H. Kameno, A. Kubo, Study on control system for active magnetic bearing considering motions of stator, Journal of System Design and Dynamics 3 (6) (2009) 954–965.
[37] C. Jarroux, J. Mahfoud, R. Dufour, B. Defoy, T. Alban, On the dynamics of rotating machinery supported by amb during base motion, in: Proceedings of ISMB15, Kitakyushu, Japon, 2016, pp. 109–115.
[38] L. A. Hawkins, B. Murphy, J. Zierer, R. Hayes, Shock and vibration testing of an amb supported energy storage flywheel, JSME International Journal Series C Mechanical Systems, Machine Elements and Manufacturing 46 (2) (2003) 429–435.
[39] G. Leilei, L. Wan, Y. Suyuan, Theoretical investigation on dynamic behavior of amb-rotor system subject to base motion disturbances, in: 12th International Symposium on Magnetic Bearings, 2010, pp. 82–90.
[40] L. A. Hawkins, R. K. Khatri, K. B. Nambiar, Test results and analytical predictions for mil-std-167 vibration testing of a direct drive compressor supported on magnetic bearings, Journal of Engineering for Gas Turbines and Power 137 (5) (2015) 052507–052507–8.
[41] M. E. Kasarda, J. Clements, A. L. Wicks, C. D. Hall, R. G. Kirk, Effect of sinusoidal base motion on a magnetic bearing, in: Proceedings of the 2000. IEEE International Conference on Control Applications. Conference Proceedings (Cat. No.00CH37162), 2000, pp. 144–149.
[42] H. F. Black, Interaction of a whirling rotor with a vibrating stator across a clearance annulus, Journal of Mechanical Engineering Science 10.
[43] A. Lingener, Investigation of reverse whirl of flexible rotor, Rakenteiden Mekaniikka 24 (1991) 3–21.
[44] A. Muszynska, P. Goldman, Chaotic responses of unbalanced rotor/bearing/stator systems with looseness or rubs, Chaos, Solitons & Fractals 5 (9) (1995) 1683–1704.
[45] F. Chu, Z. Zhang, Bifurcation and chaos in a rub impact jeffcott rotor system, Journal of Sound and Vibration 210 (1) (1998) 1–18.
[46] A. R. Bartha, Dry friction backward whirl of rotors, Phd thesis, ETH Zürich (2000).
[47] Y. S. Choi, Investigation on the whirling motion of full annular rotor rub, Journal of Sound and Vibration 258 (1) (2002) 191–198.
[48] G. Von Groll, D. J. Ewins, A mechanism of low subharmonic response in rotor/stator contact - measurements and simulations, Journal of Vibration and Acoustics 124 (3) (2002) 350–358.
[49] M. O. T. Cole, P. S. Keogh, Asynchronous periodic contact modes for rotor vibration within an annular clearance, Proceedings of the Institution of Mechanical Engineers, Part C: Journal of Mechanical Engineering Science 217 (10) (2003) 1101–1115.
[50] J. C. Wilkes, D. W. Childs, B. J. Dyck, S. G. Phillips, The numerical and experimental characteristics of multimode dry-friction whip and whirl, Journal of Engineering for Gas Turbines and Power 132 (5) (2010) 052503–052503–9.
[51] Z. Shang, J. Jiang, L. Hong, The global responses characteristics of a rotor/stator rubbing system with dry friction effects, Journal of Sound and Vibration 330 (10) (2011) 2150–2160.
[52] U. Ehehalt, O. Alber, R. Markert, G. Wegener, Experimental observations on rotor-to-stator contact, Journal of Sound and Vibration 446 (2019) 453 – 467.
[53] L. A. Hawkins, Shock analysis for a homopolar, permanent magnet bias magnetic bearing system, in: ASME Turbo Expo

1997: Power for Land, Sea and Air, no. 78712, 1997.
[54] L. Hawkins, Z. Wang, K. Nambiar, Floating Shock Platform Testing of a Magnetic Bearing Supported Chiller Compressor: Measurements and Simulation Results, Vol. Volume 7B: Structures and Dynamics of Turbo Expo: Power for Land, Sea, and Air, 2018.
[55] C. Jarroux, J. Mahfoud, B. Defoy, T. Alban, Stability of Rotating Machinery Supported on Active Magnetic Bearings Subjected to Base Excitation, Journal of Vibration and Acoustics 142 (3), 031004.
[56] Y. Su, Y. Gu, P. S. Keogh, S. Yu, G. Ren, Nonlinear dynamic simulation and parametric analysis of a rotor-amb-tdb system experiencing strong base shock excitations, Mechanism and Machine Theory 155 (2021) 104071.
[57] K. L. Cavalca, P. F. Cavalcante, E. P. Okabe, An investigation on the influence of the supporting structure on the dynamics of the rotor system, Mechanical Systems and Signal Processing 19 (1) (2005) 157–174.
[58] M. Lalanne, G. Ferraris, Rotordynamics Prediction in Engineering, John Wiley & Sons, 1998.
[59] O. Halminen, A. Kärkkäinen, J. Sopanen, A. Mikkola, Active magnetic bearing-supported rotor with misaligned cageless backup bearings: A dropdown event simulation model, Mechanical Systems and Signal Processing 50-51 (0) (2015) 692–705.
[60] T. A. Harris, Rolling Bearing Analysis, John Wiley & Sons, 2001.
[61] P. Guay, Roulements calculs, Techniques de l'ingénieur Guidage mécanique (ref. article : bm5371), fre.
[62] K.-L. Nguyen, Q.-T. Tran, M.-A. Andrianoely, L. Manin, S. Baguet, R. Dufour, M. Mahjoub, S. Menand, Nonlinear rotordynamics of a drillstring in curved wells: Models and numerical techniques, International Journal of Mechanical Sciences 166 (2020) 105225.
[63] M. Helfert, M. Ernst, R. Nordmann, B. Aeschlimann, High-speed video analysis of rotor-retainer-bearing-contacts due to failure of active magnetic bearings, in: 10th International Symposium on Magnetic Bearing, 2006.
[64] A. Palmgren, I. SKF Industries, Ball and roller bearing engineering, SKF Industries, 1959.